FABRICATION AND CHARACTERIZATION OF NANOWIRES

A Thesis

by

FRANCIS RANDALL PHILLIPS

Submitted to the Office of Graduate Studies of
Texas A&M University
in partial fulfillment of the requirements for the degree of

MASTER OF SCIENCE

August 2010

Major Subject: Materials Science and Engineering

FABRICATION AND CHARACTERIZATION OF NANOWIRES

A Thesis

by

FRANCIS RANDALL PHILLIPS

Submitted to the Office of Graduate Studies of
Texas A&M University
in partial fulfillment of the requirements for the degree of

MASTER OF SCIENCE

Approved by:

Chair of Committee,	Dimitris C. Lagoudas
Committee Members,	Xinghang Zhang
	John Whitcomb
Intercollegiate Faculty Chair,	Ibrahim Karaman

August 2010

Major Subject: Materials Science and Engineering

ABSTRACT

Fabrication and Characterization of Nanowires. (August 2010)
Francis Randall Phillips, B.S., Texas A&M University
Chair of Advisory Committee: Dr. Dimitris C. Lagoudas

The use of nanostructures has become very common throughout high-tech industries. In order to enhance the applicability of Shape Memory Alloys (SMAs) in systems such as Nano-Electromechanical Systems, the phase transformation behavior of SMA nanostructures should be explored. The primary focus of this work is on the fabrication of metallic nanowires and the characterization of the phase transformation of SMA nanowires. Various metallic nanowires are fabricated through the use of the mechanical pressure injection method. The mechanical pressure injection method is a template assisted nanowire fabrication method in which an anodized aluminum oxide (AAO) template is impregnated with liquid metal. The fabrication procedure of the AAO templates is analyzed in order to determine the effect of the various fabrication steps. Furthermore, metallic nanowires are embedded into polymeric nanofibers as a means to incorporate nanowires within other nanostructures.

The knowledge obtained through the analysis of the AAO template fabrication guides the fabrication of SMA nanowires of various diameters. The fabrication of SMA nanowires with different diameters is accomplished through the fabrication of AAO templates of varying diameters. The phase transformation behavior of the fabricated SMA nanowires is characterized through transmission electron microscopy. By analyzing the fabricated SMA nanowires, it is found that none of the fabricated SMA nanowires exhibit a size effect on the phase transformation. The lack of a size effect on the phase transition of SMA nanowires is contrary to the results for SMA nanograins, nanocrystals, and thin films, which all exhibit a size effect on the

phase transformation. The lack of a size effect is further studied through molecular dynamic simulations. These simulations show that free-standing metallic nanowires will exhibit a phase transformation when their diameters are sufficiently small. Furthermore, the application of a constraint on metallic nanowires will inhibit the phase transformation shown for unconstrained metallic nanowires. Therefore, it is concluded that free-standing SMA nanowires will exhibit a phase transformation throughout the nanoscale, but constrained SMA nanowires will reach a critical size below which the phase transformation is inhibited.

To Melissa - my wife, supporter, and best friend

ACKNOWLEDGMENTS

First, I would like to thank Dr. Dimitris Lagoudas for his support and guidance in my undergraduate and graduate education. He brought me into his research group during the summer of my junior year and has been a source of support and guidance ever since. Whether in class or in research, he would always press me harder to truly think about what I was doing. Furthermore, I would also like to thank Dr. Ibrahim Karaman and Dr. Xinghang Zhang for their help and guidance. Through weekly meetings as part of the Nanotechnology Interdisciplinary Research Team (NIRT), they have pressed me for more answers and helped me to broaden my understanding of shape memory alloys and specifically magnetic shape memory alloys materials. Additional thanks go to Dr. John Whitcomb for agreeing to be a member of my committee at the last moment. If he had not stepped up to fill this role, I would not be able to graduate at this time.

I would also like to thank Dr. Yordanos Bisrat, Dr. Hongxing Zheng, and Fang Dong for their help in fabricating and characterizing the nanowires discussed in the following thesis. Without their help, I would have been unable to complete much of the work presented in this thesis. Much of the credit for the transmission electron microscope studies goes to Dr. Luo of the Microscopy and Imaging Center (MIC). I also need to acknowledge Tom Stephens of the MIC for training me to use the scanning electron microscope. I would also like to thank Dr. Amnaya Awasthi for his guidance in learning how to perform molecular dynamic simulations. Further thanks are given to Dr. Jun Kameoka and Miao Wang for their help in fabricating the electrospun polymeric nanofibers. Furthermore, I would like to thank the National Science Foundation Integrative Graduate Education and Research Traineeship (NSF IGERT) fellowship program for helping to support my graduate school education.

My friends and colleagues deserve thanks as well. My fellow researchers Brian Lester, Brent Volk, Chris Calhoun, Dr. Darren Hartl, Justin Schick, Dr. Yves Chemisky, Patrick Klein, Dr. Parikshith Kumar, Frank Guardea, Dr. George Chatzigeorgiou, and Justin Wilkerson have provided a number of suggestions and good technical conversations which have further progressed this work. A special thank you is given to Krishnendu Haldar who was my officemate from the beginning of my graduate studies. His very presence in the office often inspired me to keep on task and focus on the work at hand. Gratitude is also extended to my friends, particularly David Brower, Andrew Brower, and Gershom Burgess for providing me a way to get relief and to relax when things got overwhelming.

Finally, I would like to thank my family. Their constant support through my education has helped me to overcome any and all challenges put in front of me. I need to thank my parents, Jonathan and Sylvie Phillips, for all they have done for me, both things that I know of and the myriad of things that I do not. Thank you for being role models through your lives. I need to thank my sister, Cynthia Phillips, who, although we have had our challenges, is there to support and discuss things. Finally, I need to thank my wife Melissa Phillips for being the great and godly woman that she is. Thank you for your constant support and friendship even when times get tough.

TABLE OF CONTENTS

CHAPTER Page

I INTRODUCTION 1

A. Literature Review 4
1. Fabrication and Use of Metallic Nanowires 5
2. Shape Memory Alloy Nanowires 7
3. Molecular Dynamics Simulations 9
B. Research Objectives 12

II FABRICATION AND UTILIZATION OF NANOWIRES 14

A. Experimental Procedures 14
1. Anodized Aluminum Oxide Template Fabrication . . . 15
2. Extrusion of Metallic Nanowires 17
3. Release of Metallic Nanowires 18
4. Electrospinning of Metallic Nanowires into Polymeric Nanofibers 20
B. Results 21
1. Effect of AAO Fabrication Steps 22
2. Fabrication of AAO Templates of Various Diameters . 28
3. Electrospinning of Metallic Nanowires in Polymeric Nanofibers 31
C. Conclusion 33

III SMA NANOWIRES 36

A. Experimental Procedures 36
1. Fabrication of the Bulk InTl Alloy 37
2. Characterization of InTl Nanowires 37
B. Results 38
1. Bulk In-21at%Tl and In-26at%Tl Alloys 39
2. In-21at%Tl Nanowires 41
C. Conclusion 48

IV MOLECULAR DYNAMICS SIMULATIONS OF NANOSTRUCTURES 53

A. Molecular Dynamics 53
1. Modified Embedded Atom Method 54

CHAPTER Page

2. Numerical Integration 55
B. Preliminary Simulations and Results 57
1. Gold 57
2. Indium and Thallium 60
C. Dimensionality Parametric Study 61
D. Effect of Constraints on Phase Transformation 73
E. Conclusion 75

V CONCLUSIONS 79

REFERENCES 84

VITA 94

LIST OF TABLES

TABLE		Page
I	AAO template fabrication procedure	16
II	Anodization parameters for fabrication of various nanowire diameter	30
III	Composition of various 60nm diameter nanowires. Target nanowire composition is 79at%In-21at%Tl	43
IV	MD simulation structures and dimensions	63
V	MD simulation steps for case 1	64
VI	MD simulation steps for case 2	65

LIST OF FIGURES

FIGURE		Page
1	Top view of finished AAO template.	17
2	Experimental set-up for the extrusion of the metallic nanowires.	19
3	Schematic setup of a typical electrospinning system. For the present study, the precursor solution is a mixture of SOG, PVP and Sn nanowires.	22
4	Top view of finished AAO template using the original fabrication parameters.	23
5	AAO template after 1^{st} anodization.	24
6	AAO template after 2^{nd} anodization.	26
7	AAO template after 1^{st} pore widening.	27
8	AAO template after 2^{nd} and 3^{rd} pore widening.	29
9	AAO templates with varying nominal nanopore diameter.	31
10	Electrospun silica nanofiber with embedded tin nanowire.	32
11	Bundle of Sn nanowires within a silica nanofiber.	34
12	XRD patterns at room temperature of In-21at%Tl and In-26at%Tl bulk alloys.	39
13	XRD patterns of In-21at%Tl bulk at various temperatures.	41
14	In-21at%Tl nanowires in cross-section of an AAO template and EDS of a nanowire.	42
15	SAED pattern of 650 diameter In-21at%Tl nanowire at room temperature.	44
16	TEM dark field micrograph of In-21at%Tl nanowire at room temperature with a diameter of 260 nm. The lines indicate twin boundaries.	45

FIGURE Page

17 Group of In-21at%Tl nanowires with an average diameter of 75 nm. . 47

18 In-21at%Tl nanowire with a diameter of 70 nm. 48

19 Group of In-21at%Tl nanowires with a diameter of 15 nm. 49

20 TEM and SAED results for 10 nm diameter In-21at%Tl nanowires. . 50

21 Density versus pressure for bulk Au. 59

22 Case 1: MD simulation of Au nanowire at different time steps (arrows indicate transformation fronts). 66

23 Case 1: MD simulation of Au nanosphere showing different time steps. 66

24 Case 1: MD simulation of Au thin film at different time steps. 67

25 Case 2: MD simulation of Au nanosphere at different time steps. . . 69

26 Case 2: MD simulation of Au nanowire at different time steps (arrows indicate transformation fronts). 70

27 Case 2: MD simulation of Au thin film at different time steps. 71

28 Ni nanowire showing transformation (arrows indicate transformation fronts). 73

29 Nanowire used to simulate effect of constraints on nanostructures. . . 74

30 Simulation of Au nanowire with a constraint. Simulation does not show phase transformation (compare to Fig. 26). 76

CHAPTER I

INTRODUCTION

Over the last 20 years, a significant trend has emerged showing the need for multifunctionality of material systems. The trend for increased multifunctionality is most clearly demonstrated by the amount of research which has been performed on materials such as piezoelectrics, magnetostrictives, thermoelectrics, electrostrictives, and shape memory materials [1]. These materials are part of a family of materials called multifunctional materials, that is, these materials exhibit a coupling between various forms of energy. For instance, piezoelectrics couple mechanical and electrical effects. Thermoelectrics couple thermal and electrical effects. Shape memory materials couple thermal and mechanical effects. These materials are becoming more common throughout commercial products, ranging from piezoelectric sensors as touchscreens, chemical sensors, and biosensors [2, 3], to shape memory alloy as dental archwires and as frames for eyeglasses [4].

Of the multifunctional material family, Shape Memory Alloys (SMAs) have the highest actuation energy density, that is the highest amount of actuation stress and strain combination [4]. One distinctive property of SMAs is their reversible phase transformation from a high temperature phase known as austenite to a low temperature phase known as martensite. The transformation from austenite to martensite is called forward transformation and is characterized by the martensite start (M_s) and martensite finish (M_f) temperatures. The transformation from martensite to austenite is called reverse transformation and is characterized by the austenite start (A_s) and austenite finish (A_f) temperatures. The start and finish temperatures corre-

---

The journal model is *International Journal of Engineering Science*.

spond to those temperatures at which the SMA starts and finishes transforming into the new phase. Typically, the austenitic phase has a cubic crystal structure, while the martensitic phase has a monoclinic crystal structure. When under zero stress, a SMA which is cooled from austenite into martensite will have a self-accommodated structure. Self-accommodated martensite has no net change in shape or volume relative to austenite. The ability of the microstructure to form twins is responsible for the lack of shape and volume change [4, 5, 6].

Shape Memory Alloys can be fabricated from a number of different alloys. The properties of the various SMAs are directly correlated to the chemical composition of the alloy from which they are made. Certain alloys which exhibit the properties of SMAs include Nickel Titanium (NiTi), Copper Aluminum Nickel (CuAlNi), Nickel Aluminum (NiAl), and Indium Thallium (InTl).

One drawback to the use of SMAs is the relatively low actuation frequency exhibited by bulk SMA structures. For bulk SMA structures, the frequency of actuation is typically less than 1 Hz. In general, the frequency of actuation exhibited by SMAs is lower than other multifunctional materials such as piezoelectrics (up to 1 MHz) or electrostrictives (up to 1 kHz). The relatively low actuation frequency of SMAs is one reason why SMAs have not been used in as many applications as other multifunctional materials. The primary reason why the actuation frequency of SMAs is low is due to the latent heat of transformation. In order to allow for both the forward and reverse phase transformation, the latent heat must be dissipated quickly. However, bulk structures of SMA do not allow for sufficiently quick release of the latent heat. One possible solution to the dissipation of latent heat problem is to reduce the size of an SMA actuator to the nanoscale. It is expected that due to the small size of nanoscale SMAs, the latent heat of transformation will be able to dissipate much faster through the SMA and therefore allow for a much higher frequency of

actuation. Such nanoscale actuators could have widespread use in the field of high-tech electronics. The field of high-tech electronics has seen tremendous increases in computational power throughout the last 50 years while at the same time reducing the size of their components. The miniaturization of electrical components has allowed for much faster transmission of data while at the same time allowing for greater heat dissipation of the components. Recent years have seen the invention and use of a number of miniaturized electromechanical systems. These systems include both micro-electromechanical systems [7, 8, 9] as well as nano-electromechanical systems [10, 11, 12, 13]. The future use of nanoscale SMA actuators in such systems will require an understanding of the properties of nanoscale SMAs.

The use of nanoscale SMAs presents a new field of study to analyze the behavior of SMAs when the dimensions are reduced to the nanoscale. Since typically the most attractive property of SMAs is their ability to transform, it is therefore important to know how the reduction in size to the nanoscale will effect the phase transformation. There have been several studies performed to date that have attempted to illuminate the nanoscale behavior of nanoscale SMAs. These studies have investigated nanograins, nanocrystals, and thin films. As will be discussed below, these studies found that there is a limiting size below which the phase transformation is inhibited [14, 15, 16, 17, 18, 19, 20]. However no studies of the phase transformation of SMA nanowires have yet been performed. There have been several studies which use molecular dynamics to show that various metals which do not exhibit a phase transformation in the bulk do exhibit a phase transformation in nanowires [21, 22, 23, 24, 25, 26]. Since there is a definite size effect that exists for SMA nanograins, nanocrystals, and thin films, the primary question to be addressed in this thesis is whether there also exists a size effect on the phase transformation of SMA nanowires.

The goal of the following work is to investigate the existence of a size effect on the

phase transformation of SMA nanowires, both experimentally and numerically. In the following study, the first step will be to develop an understanding of how the nanowires are fabricated. The fabrication of nanowires will be analyzed through the fabrication on Tin nanowires. Using the knowledge of the fabrication procedure gained through the fabrication of Tin nanowires, SMA nanowires composed of Indium-Thallium will be fabricated. The reason for the selection of Indium-Thallium as the SMA is due to the low melting temperature of Indium-Thallium. As will be explained below, the nanowire fabrication procedure requires a low melting temperature for the metal from which the nanowires are fabricated. The phase transformation of various Indium-Thallium nanowires is investigated experimentally in order to determine the existence of a size effect on the phase transformation. Results obtained experimentally are also compared to numerical results obtained through Molecular Dynamics simulations in an attempt to gain further insight into the experimental behavior observed.

A. Literature Review

The body of this thesis will be divided into three chapters, namely the fabrication and utilization nanowires, the fabrication and characterization of SMA nanowires, and Molecular Dynamics (MD) simulations of nanostructures. The nanowire fabrication procedure presented in Ch. II will be used to fabricate the SMA nanowires characterized in Ch. III. Also, due to the results obtained in Ch. III, it was decided to undertaken a numerical study using MD simulations (as described in Ch. IV) to gain a clearer understanding of the results obtained in Ch. III.

1. Fabrication and Use of Metallic Nanowires

The fabrication of metallic nanowires has been achieved through a number of different methods, including shadow sputtering [27, 28], nanolithographic techniques such as electron-beam lithography and focused-ion-beam lithography [29, 30, 31], proximal-probe patterning [32, 33], and template synthesis [34, 35, 36, 37, 38]. Of the above listed nanowire fabrication methodologies, the template synthesis methods have been heavily investigated due to the low cost, simplicity, and repeatability of these methods.

One such template synthesis method which has been investigated is the mechanical pressure injection method [39, 40, 41]. This method has been applied to the fabrication of a number of different nanowires ranging from pure metals, such as Bismuth (Bi) [42], to alloys, including Gold-Silicon (Au-Si) [43]. This method relies on the use of a template into which liquid metal is injected. According to Chen et al., template filling ratios near 100% can be achieved using this method [40]. Therefore, this method is considered to be a high yield nanowire fabrication method. The primary drawback of this method is the use of an aluminum oxide template. The aluminum oxide templates are fabricated using aluminum as a base material. Due to the low melting temperature of aluminum (≈ 650 °C), only metals with a lower melting temperature can be used to fabricate nanowires using this technique. Therefore the following study uses the mechanical pressure injection method to fabricate all of the nanowires presented.

In order to pursue this fabrication technique, an understanding of the fabrication of the anodized aluminum oxide (AAO) templates is necessary. The fabrication of such templates has received significant interest since Masuda and Fukuda first reported obtaining hexagonal close packed highly ordered nanoporous alumina in 1995 [36]. Since then a number of anodization methods have been used to obtain

nanoporous alumina with nanopore diameters from 15-500 nm [40, 44, 45, 46, 47, 48]. Many of these methods utilize what is known as a two step anodization procedure. This allows for a more uniform and controlled growth of the nanopores. The wide variety of nanopore sizes is important for the proposed work in InTl nanowires due to the need for a variety of nanowire diameters. Zhang et al. have directly studied the effect of changing the anodization parameters [48]. In their study, they changed the temperature and anodization voltage and noticed a change in the nanopore diameter and interpore distance. However, in the studies cited above, no step by step study of the full AAO template fabrication process has been performed. These studies described the starting and ending states of the alumina, as well as how they achieve the end state, but in-between steps were not analyzed. Thus, a step by step study of the fabrication procedure for 60 nm nanopore diameter AAO templates was conducted. Furthermore, through analysis of the fabrication procedure, various parameters in the AAO template fabrication procedure was modified, in accordance with the literature cited above, to fabricate AAO templates with various nanopore diameters.

The fabrication of nanowires is only one step towards the use of such structures. It is also worthwhile to find uses and deposition techniques for such nanowires. One solution to the deposition issue is to embed nanowires in polymeric nanofibers by means of an electrospinning process. The process of electrospinning has been well studied for polymeric systems, dating back to 1934 [49]. Since then, electrospinning of polymeric nanofibers has been employed in a number of different applications [50, 51]. However, the incorporation of metallic nanowires into polymeric nanofibers fabricated through the electrospinning process has not yet been accomplished. This study uses electrospinning to embed Sn nanowires into silica nanofibers as a method to deposit and use metallic nanowires.

2. Shape Memory Alloy Nanowires

Various studies have been performed to date in an attempt to illuminate that phase transformation properties of nanoscale SMA structures. These studies have shown experimentally that SMAs which exhibit a reversible phase transformation at the macroscale no longer exhibit a phase transformation at the nanoscale. For example, Malygin found that $FeNi_{31}C_{0.28}$ nanograins no longer exhibit a phase transformation once the nanograins became smaller than $\approx$ 20 nm [14]. Additionally, Waitz et al. derived a model for spherical nanograins of Nickel Titanium (NiTi) which shows a significant rise in the surface energy as a function of the grain size [15]. The results of Waitz et al. indicate a large increase in the energy barrier against phase transformation as the grain size is reduced below 75 nm. Furthermore, their results indicate that the energy barrier becomes too large to overcome for grain sizes less than 50 nm. Wan and Komvopoulos found that the phase transformation of TiNi thin films is completely suppressed when the thickness of the thin films is below 50 nm [16]. Several other studies have been performed on various other SMA nanograins, nanocrystals, and thin films [17, 18, 19, 20]. In addition, some modeling work has been performed on SMAs at the nanoscale [52, 53]. All of the cited studies have shown the existence of a size effect on the phase transformation of SMAs. However, an experimental study of the size effect on the phase transformation of SMA nanowires has not yet been performed. The following study will investigate the existence of a size effect on an SMA nanowire by varying the diameter of fabricated nanowires from 650 nm to 10 nm.

In order to satisfy the constraints of the nanowire fabrication method that has been chosen, namely the mechanical pressure injection method, the size effect on the phase transformation of SMA nanowires is investigated on an Indium Thallium alloy.

According to Nittono and Koyama, InTl alloys with 18at% to 30at% Tl form SMAs [54]. For this range of compositions, the melting temperature is approximately 160 °C [55]. The wide range of compositions of InTl which forms a SMA is ideal for the proposed study since such a range allows for minor variation of the composition without large differences in the properties of the resulting alloy. This is in direct contrast to other SMAs such as NiTi, where the composition must be very tightly controlled. A slight shift in composition from Ti-50at%Ni to Ti-51at%Ni results in a shift of A_f from over 100 °C to below 0 °C [56]. In contrast, changing the composition of InTl alloys by 1at% shifts the transformation temperature by approximately 28 °C [57]. Based on results from Jaglinski et al., the transformation temperature for an alloy of In-21at%Tl is approximately 50°C, indicating that the alloy should be in the martensitic phase at room temperature [58]. Also, in contrast to other SMAs where the difference between A_f and M_f could be larger than 100 °C, the difference for InTl alloys is 1-2 °C [59].

For all compositions of InTl which form a SMA, the phase transformation is from an austenitic face-centered cubic (FCC) crystal structure to a martensitic face-centered tetragonal (FCT) crystal stucture [60]. The phase transformation in indium-thallium allows the formation of three martensitic variants where each variant is a rotation of the other variants. The Bain matrix or transformation matrix, U, is given by:

$$U = \begin{bmatrix} \beta & 0 & 0 \\ 0 & \alpha & 0 \\ 0 & 0 & \alpha \end{bmatrix} \tag{1.1}$$

where $\alpha = 0.9889$ and $\beta = 1.0212$ [61]. In all of the cited studies, the measurements

were made for the bulk alloys.

3. Molecular Dynamics Simulations

The use of molecular mechanics and *ab-initio* calculations have become widespread tools to investigate the properties of nano-materials. It is therefore of interest to the current study to use such methods to simulate the behavior of nanosystems in order to provide a means to verify and explain any behavior obtained through the experimental studies performed for the SMA nanowires. *Ab-initio* methods, including density functional theory (DFT), allow for the calculation of various properties of atomic systems [62, 63, 64, 65]. However, these methods typically only allow for the simulation of at most hundreds of atoms. Furthermore, all calculations performed by *ab-initio* methods are performed at 0 K, indicating that no thermal effects are directly taken into account during the simulations. Therefore, such methods are inappropriate for the calculations to be performed in the following study. Also, stochastic methods such as Monte Carlo are not appropriate this study since the motion of the atoms is of primary concern [66].

The field of molecular mechanics can be divided into two categories, namely molecular statics and molecular dynamics (MD). These methods allow for the simulation of a larger number of atoms due to the fact that molecular mechanics uses a general electron density for each atom instead of attempting to calculate the exact electronic structure of each atom. One drawback to the use of molecular statics is that all simulations performed using molecular statics are at 0 K [67, 68]. Therefore, molecular statics cannot be used for the current study either. On the other hand. MD simulations allow for the movement of atoms over fixed time intervals and at finite temperatures. The systems under consideration in this study all operate at a finite temperature and therefore MD was selected as the method of choice to simulate

the nanostructures under consideration.

A common package which has received extensive use in MD simulations is known as the Large-scale Atomic/Molecular Massively Parallel Simulator (LAMMPS) [69]. Over 500 reviewed papers which use LAMMPS have been published in peer-reviewed journals, including several which investigate various solid-solid phase transformations [70, 71]. One reason why this program has been extensively used is the fact that it allows for the use of a number of different input potential types. These potentials determine how MD programs treat the atoms and the way in which atoms interact. Several different types of potentials have been developed and each have their own strengths and weaknesses. One potential which works particularly well and has been used extensively to model metals is the Embedded Atom Method (EAM) potential [72]. This method and potential were developed by Daw and Baskes [73]. A distinct drawback to this potential, however, is that it does not account for angular bonding. In order to account for this deficiency, as well as certain other deficiencies, Baskes modified the original EAM and derived the Modified Embedded Atom Method (MEAM) [74]. This method has also become widely used [75]. Due to the fact that the MEAM allows for directional bonding, and since the phase transformation of SMAs results in a change in the bond angles, the MEAM was used in the simulations performed for this study. A more in-depth look at how LAMMPS uses the MEAM to simulate systems is provided in Ch. IV.

It has been previously shown that certain systems exhibit a reversible phase transformation at the nanoscale. Specifically, using the MEAM, authors have shown the nanowires of Gold (Au), Silver (Ag), and Copper (Cu) exhibit a crystal structure transformation [21, 22, 23, 24, 25, 26]. The transformations observed in these systems are not typical of the bulk materials from which they are made. According to Liang et al. [21], a reversible transformation has been observed using MD simulations

for Cu nanowires with size ranges between 1.76 and 3.39 nm. The transformation exhibits recoverable strains of up to 50% for Cu nanowires. It should be noted, however, that for Cu nanowires, the transformation is due to twinning within the FCC phase rather than changing the crystal structure. For Ag, it has been shown by Park and Ji [22] that Ag nanowires with square cross sections of 2.045nm in length exhibit a reversible transformation from $< 100 >$ FCC to $< 110 >/\{111\}$ FCC. This transformation occurs at 400 K. Upon application of a sufficient load at 500 K, the Ag nanowire returned to its initial $< 100 >$ orientation and subsequent release of the load returned the wire to the $< 110 >/\{111\}$ orientation. This transformation is commonly known as pseudoelastic behavior and is common among SMAs. However, as with Cu, it should be noted that the transformation shown by Park and Ji for Ag nanowires is only a reorientation of the FCC crystal structure through twinning.

For Au, Diao et al. have shown that nanowires with a square cross-section exhibit a two stage phase transformation from $< 100 >$ FCC to BCC and then from BCC to $< 110 >$ FCC [23]. Since this is a solid to solid crystal structure transformation, this is therefore a similar phase transformation to that exhibited by SMAs. Similar results have also been found for Au nano-films [76]. In the paper by Hasmy et al. on nanofilms, the authors investigate a number of different nano-films and find that various 4d and 5d transition metals exhibit a phase transformation when the thickness of the films is very small, on the order of 8 atomic layers. Hasmy et al. use these results and claim that such results can be expanded to include the the behavior of nano-films of other metallic systems.

B. Research Objectives

The three primary research objectives addressed in this thesis are the fabrication and use of nanowires, the characterization of SMA nanowires, and MD simulations of phase transformations in nanostructures. These research objectives build upon one another in that nanowires must first be fabricated prior to characterization. Furthermore, the MD simulations of the phase transformations in nanostructures are based upon the results obtained through the characterization of the SMA nanowires. The three research objectives mentioned above will be further discussed below.

The fabrication and use of nanowires rely on a method known as the mechanical pressure injection method. To understanding how the mechanical pressure injection method works as well as how to control the diameter of the resulting nanowires, it is necessary to first comprehend the AAO fabrication procedure. Understanding the AAO template fabrication procedure will be achieved through a step by step study of the fabrication procedure of an AAO template. Furthermore, knowing what each step in the AAO template fabrication procedure accomplishes will allow for the fabrication of AAO templates of various nanopore diameters which will be necessary for study of InTl nanowires. The use of metallic nanowires within other structures will also require the ability to deposit the nanowires individually. Therefore, the following study will attempt to embed metallic nanowires into polymeric nanofibers through an electrospinning process. Such a method will provide a means to use metallic nanowires in other structures. Both of these topics will be addressed in Ch. II.

The characterization of SMA nanowires will address the existence of a size effect on the phase transformation of SMA nanowires. Due to the nanowire fabrication procedure, the SMA selected on which to perform the size effect study for SMA nanowires is InTl. Therefore, prior to characterizing the nanowire phase transformation behav-

ior of this alloy, it will also be necessary to characterize the phase transformation behavior of bulk InTl. Characterizing the phase transformation will be done for two different alloys of InTl, namely In-21at%Tl and In-26at%Tl. The reason for fabricating both of these bulk alloys is so that at least one of the alloys fabricated will be in the martensitic phase at room temperature. The importance of having a bulk alloy which is in the martensitic state at room temperature is that it will aid in the determination of a size efect on the phase transformation temperature. Upon selection of the appropriate InTl alloy, SMA nanowires of various diameters will be fabricated using the mechanical pressure injection method. The phase transformation of the fabricated SMA nanowires will then be characterized in order to determine if there exists a size effect on the phase transformation of SMA nanowires. These topics will be discussed in Ch. III.

The use of MD simulations allows for the simulation of various nanostructures which would otherwise be nearly impossible to fabricate experimentally. Therefore, utilizing MD simulations, the experimental study performed for SMA nanowires will be further expanded. The primary differences between the fabricated SMA nanowires and previous experimental studies on SMA nanostructures are the dimensionality and the constraints applied on the SMA nanostructures. Therefore, the effect of dimensionality and constraints on the phase transformation of nanostructures will be explored in Ch. IV.

CHAPTER II

FABRICATION AND UTILIZATION OF NANOWIRES

In the current chapter, the fabrication and utilization of metallic nanowires is discussed. First the nanowire fabrication procedure, known as the mechanical pressure injection method, is presented. The mechanical pressure injection method injects liquid metal into a nanoporous anodized aluminum oxide template and allows the liquid metal to cool and therefore form nanowires. Second, the fabrication steps of the anodized aluminum oxide templates are then analyzed in order to determine the effect of the fabrication steps. Third, various parameters in the anodized aluminum oxide template fabrication procedure will be modified in order to fabricate anodized aluminum oxide templates containing different nominal nanopore diameters. Finally, the electrospinning of metallic nanowires into polymeric nanofibers is presented.

A. Experimental Procedures

In the following section, the experimental procedures used to fabricate and utilize metallic nanowires are presented. As mentioned, the mechanical pressure injection method is used to fabricate all nanowires in the following study. The mechanical pressure injection method can be divided into three parts: anodized aluminum oxide (AAO) template fabrication, nanowire extrusion, and nanowire release. In the first part of the mechanical pressure injection method, an AAO template is fabricated using an anodization, pore widening, and heat treatment procedure. The AAO template is nanoporous and these pores serve to guide the formation of the nanowires. In the second part, liquid metal is injected into the template and allowed to solidify. The last part of the nanowire fabrication procedure is to dissolve the AAO, thereby releasing the nanowires. Also presented in the experimental procedure is the method

utilized to embed metallic nanowires into polymeric nanofibers. The following study will utilize an electrospinning process to embed Sn nanowires into silica nanofibers. Unless otherwise noted, all steps performed in the fabrication and utilization of the nanowires were performed at room temperature.

1. Anodized Aluminum Oxide Template Fabrication

The AAO template fabrication uses a two step anodization procedure. The following procedure results in the fabrication of AAO templates with a nominal diameter of 60 nm. Throughout the AAO template fabrication procedure described below, the aluminum foil is rinsed with deionised water and dried between all steps of the following AAO template fabrication procedure. First, a piece of aluminum foil (approximately 1 in by 1 in) is cut from a bulk piece of aluminum foil purchased from Alfa Aesar (99.9+% pure), degreased overnight in an acetone bath, followed by ultrasonic cleaning in the acetone bath and removal of any oxide layer with 3.0 M NaOH. The cleaned aluminum foil is subsequently anodized using 3vol% oxalic acid as the electrolyte at 40 V. The duration of the first anodization is 1 hour.

After the first anodization, nanopores have formed in the aluminum foil, however these nanopores are not well organized and are unsuitable for the fabrication of nanowires. Therefore, the anodized layer is dissolved in a mixture of 0.4 M phosphoric acid and 0.2 M chromic acid for 1 hour. Removal of the first anodization layer should leave behind a textured surface from which the nanopores of the second anodization will grow. Using the same anodization parameters as the first anodization, the aluminum foil is anodized a second time. The depth of the nanopores is primarily determined by the length of the second anodization. After the second anodization, the AAO has formed above an underlying aluminum substrate and the AAO and aluminum substrate are cumulatively called the AAO template. The final step in

Table I. AAO template fabrication procedure

Step	*Solution Used and Voltage*	*Time*	*Temperature (°C)*
Clean Aluminum	Acetone Bath	N/A	RT
1^{st} Anodization	0.3 M $C_2O_4H_2$, 40 V	1 h	RT
Dissolve	0.4 M H_3PO_4 and 0.2 M H_2CrO_4	1 h	RT
2^{nd} Anodization	0.3 M $C_2O_4H_2$, 40 V	2 h	RT
Pore Widen	5vol%H_3PO_4	15 min	RT
Heat Treat		8 h	550
Pore Widen	5vol%H_3PO_4	80 min	RT
Heat Treat		8 h	550
Pore Widen	5vol%H_3PO_4	80 min	RT

RT: Room Temperature

the AAO template fabrication procedure is to widen the fabricated pores. First, the AAO template is etched in 5vol% phosphoric acid for 15 minutes. Then, the AAO template is subjected to a heat treatment at 550°C for 8 hours. The AAO template is subsequently etched again in 5vol% phosphoric acid for 80 minutes and heat treated again at 550°C for 8 hours. Finally, the AAO template is etched again in 5vol% phosphoric acid for 80 minutes.

The above procedure, summarized in Table I, results in the fabrication of an AAO layer above an underlying aluminum substrate. The aluminum substrate remains attached to the AAO layer in order to provide support and ensure structural integrity of the AAO throughout the rest of the nanowire fabrication process. A combined top and cross-sectional view of a finished AAO template is shown in Fig. 1.

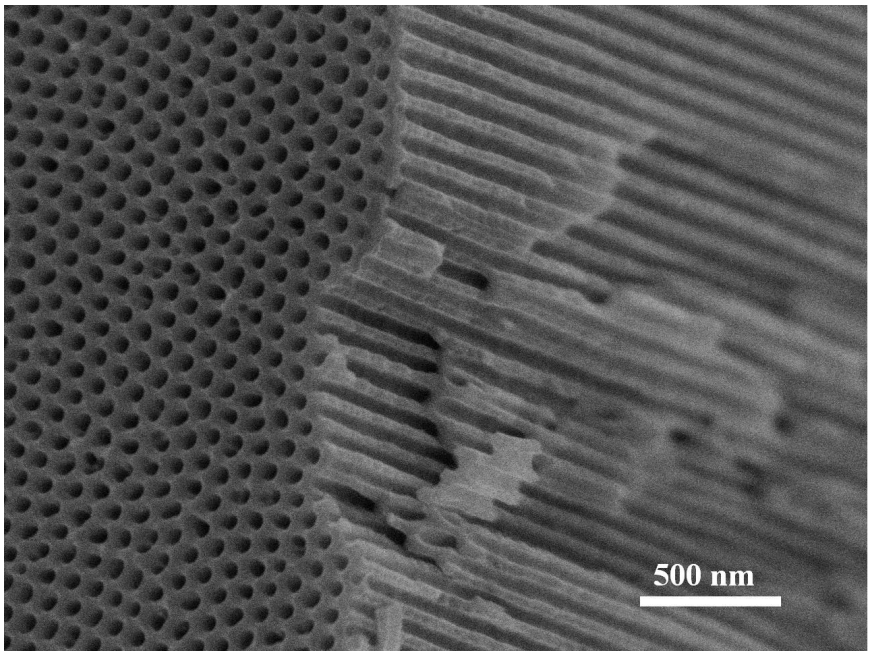

Fig. 1. Top view of finished AAO template.

2. Extrusion of Metallic Nanowires

Nanowires are fabricated by placing the AAO template into a mold along with a film of metal. The film of metal is cut from a piece of bulk metal. The first metallic nanowires which were fabricated in this study were fabricated from tin (Sn) and the bulk Sn is fabricated by placing high purity Sn granules (99.9% pure) in a quartz tube. The filled tube is first subjected to a vacuum, then flushed with argon, and then the vacuum is restarted prior to sealing the tube. The tube is then heated uniformly until the granules melt. The molten Sn is allowed to solidify prior to release of the vacuum and removal of the Sn ingot from the tube.

The mold containing the AAO template and the film of metal is placed into a chamber made of stainless steel, as shown in Fig. 2.a. The chamber is sealed and connected to a vacuum pump in order to evacuate the chamber. The chamber is then flushed with argon gas in order to ensure an inert environment and the vacuum is

restarted. The chamber is heated by a hot plate to approximately melting point of the metal, however the melting point of the metal must be sufficiently low to prevent the contamination of the nanowires by the underlying aluminum substrate, thereby necessitating the use of metals with low melting temperatures. The temperature inside the chamber is verified by inserting a thermocouple into the top of the chamber. Upon reaching the melting temperature of the metal from which the nanowires will be fabricated, the chamber is removed from the hot plate and placed on a hydraulic jack, as shown in Fig. 2.b. The hydraulic jack applies approximately 10 tons of pressure on the molten metal by an arm of the chamber and thus injects the molten metal into the nanopores of the AAO template. The reason that a hydraulic jack must be used to impregnate the liquid metal into the AAO template is due to the highly hydrophobic nature of the AAO template, which will otherwise tend to keep the liquid metal out of the nanopores of the AAO template [77]. Immediately after application of pressure by the hydraulic jack, the entire chamber is placed in a water bath to allow the nanowires to solidify inside the AAO template nanopores. After sufficient cooling (4-5 minutes), the chamber is disassembled and the AAO template with injected metallic nanowires is removed.

3. Release of Metallic Nanowires

After the injection and cooling process, the fabricated metallic nanowires are embedded within the AAO template. In order to release the nanowires from the AAO template, the AAO template is cut into small pieces and placed in a vial along with a bath of 0.4 M phosphoric acid and 0.2 M chromic acid. The acidic solution attacks the aluminum oxide, hence dissolving it while leaving the nanowires relatively unharmed. To release the nanowires in the acidic solution at room temperature requires approximately 1 week to completely dissolve the AAO and thus release the nanowires.

(a) Bottom Half of Extrusion Chamber showing mold inside

(b) Chamber in Hydraulic Jack

Fig. 2. Experimental set-up for the extrusion of the metallic nanowires.

The resulting released nanowires have the same length as the depth of the nanopores.

Alternative methods to release the nanowires have been tried. One simple method is to sonicate the vial containing the AAO template, nanowires, and acidic solution periodically. By sonicating the vials approximately every 6 hours for 20 seconds, the time to fully release the nanowires can be cut down to 24 hours. However, sonicating the vials severely harms the nanowires; instead of being as long as the nanopores, the Sn nanowires are broken into several shorter segments. Another method used to accelerate the release of the nanowires is to increase the temperature of the bath from room temperature to approximately 60 °C. Heating the acidic solution reduces the dissolution time to approximately 2 days. However, as heating the acidic solution results in the acid being more aggressive, the acid tends to cause the formation of an oxide layer on the nanowires.

The dissolution of the AAO releases the nanowires, leaving the nanowires in the

acidic bath. To prevent the formation of any further oxide layer on the surface of the nanowires, the acidic bath must now be removed from the vial containing the nanowires. The aluminum substrate which was attached to the bottom of the AAO is first removed from the acidic bath using tweezers. Then the acidic bath is removed through a solution removal procedure consisting of centrifuging the vials, removing part of the acidic bath from the vial, and then refilling the vials with deionized water. The use of a centrifuge causes the nanowires to deposit on the side of the vial and therefore reduces the amount of nanowires removed from the vial when part of the acidic bath is removed. The use of the centrifuge does damage the nanowires somewhat since it causes a high acceleration on the nanowires, however the damage caused by the centrifuge is significantly lower than the damage caused by sonication. The solution removal procedure is repeated several times (8-10) until the mixture is nearly free of the acidic solution.

Finally, the solution removal procedure is repeated to replace the deionized water with ethanol. Again, the solution removal procedure is repeated several times (8-10). The reason for placing the nanowires in ethanol is such that the nanowires are in an inert environment where the nanowires will not be oxidized. For use in the electrospinning process, the ethanol is replaced by isopropanol in a similar fashion as described above. The isopropanol is necessary due to certain requirements of the electrospinning process.

4. Electrospinning of Metallic Nanowires into Polymeric Nanofibers

The process of electrospinning metallic nanowires into polymeric nanofibers was first performed using Sn nanowires fabricated as described above. The fabricated and released Sn nanowires which are located in a isopropanol bath are first sonicated in order to disperse the nanowires throughout the isopropanol. The sonication step also helps

to decrease the bundling of the nanowires, which is important as will be discussed in the results section. These nanowires are then mixed into a mixture of spin-on glass (SOG) intermediate coating IC1-200 (Futurex, Inc) solution and polyvinylpyrrolidone (PVP) (Aldrich, Molecular Weight=1,300,000). The entire solution is stirred with a magnetic bar continuously until the solution is used in the electrospinning process. Stirring the solution ensures that the metallic nanowires are dispersed throughout the solution.

The first step in the electrospinning process is to place the solution prepared above into a plastic syringe with a metal needle at the end. A grounded collecter plate is placed several centimeters from the tip of the needle. During electrospinning, the collector plate rotates in order to prevent accumulation of the electrospun nanofiber at one location. By applying a sufficiently high voltage on the needle, the surface tension of the solution is overcome, and a liquid jet is extracted from the needle and is sent spinning towards the grounded collector plate. A graphic representation of the electrospinning process described is presented in Fig. 3. The electrospinning work was conducted in the Nanostructure Science and Engineering Lab.

B. Results

The following results investigated the fabrication of the AAO templates and the fabrication of silica nanofibers with coaxially spun Sn nanowires. The fabrication of the AAO templates is of primary importance to the fabrication of metallic nanowires using the mechanical pressure injection method as the size of the nanopores in the AAO templates determines the size of the resulting nanowires. It is therefore necessary to understand the entire AAO template fabrication procedure. Furthermore, by understanding how the AAO templates are fabricated, changes to the fabrication

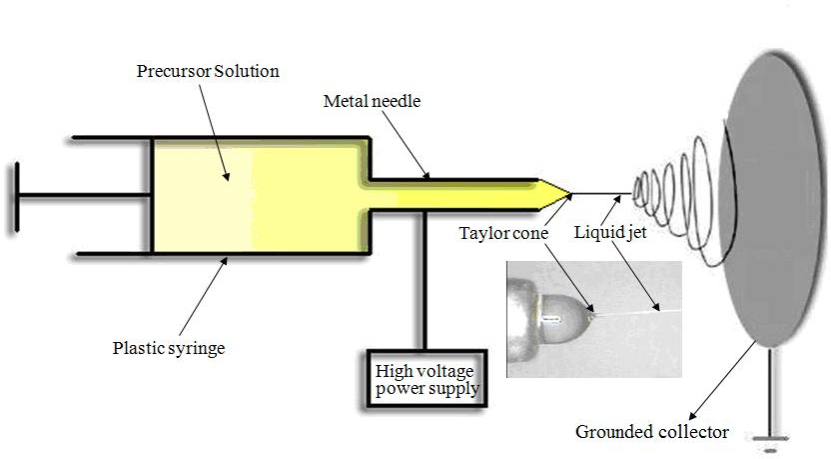

Fig. 3. Schematic setup of a typical electrospinning system. For the present study, the precursor solution is a mixture of SOG, PVP and Sn nanowires.

method can be implemented to vary the size of the nanopores in the AAO templates. Varying the size of the nanopores will allow for the fabrication of metallic nanowires of various diameters. As AAO templates of various nanopore diameter will be used in Ch. III, the effect of varying the AAO template fabrication parameters will also be studied. Also, as described above, the electrospinning of metallic nanowires into polymeric nanofibers should enhance the electrical conductivity of the polymeric nanofibers. Therefore, the electrical conductivity of silica nanofibers electrospun with Sn nanowires was studied.

1. Effect of AAO Fabrication Steps

As described previously, the fabrication of the AAO templates is based on a two-step anodization procedure of aluminum foil. An understanding of the effects of each step in the fabrication procedure is necessary in order to modify the AAO template fabrication procedure as will be needed when fabricating AAO templates of other diameters in Ch. III. In the following discussion, all size measurements were made

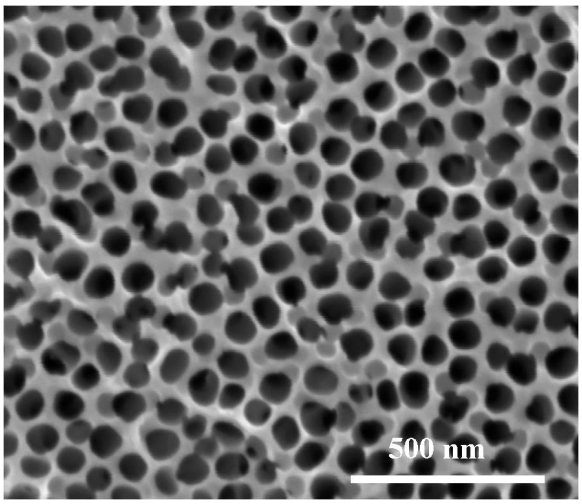

Fig. 4. Top view of finished AAO template using the original fabrication parameters.

using ImageJ [78].

It was observed through SEM investigation that the AAO templates fabricated using the AAO template fabrication procedure as described previously resulted in the formation of an irregular surface structure as shown in Fig. 4. Through further SEM observation of the various steps in the AAO fabrication process, it was determined that the root cause of the irregular surface of the finished template was an inadequate dissolving step after the first anodization. Therefore, to correct the inadequate dissolving step, new templates were fabricated using the same AAO template fabrication parameters except that the temperature of the dissolving step was raised to 60 °C instead of room temperature and lasted for 4 hours instead of 1 hour. Using these new parameters for the dissolving step, the following is an analysis of the entire AAO template fabrication procedure.

In the first anodization, nanopores start to form at imperfection sites on the aluminum surface. Since imperfections are located randomly across the surface of the aluminum, the nanopores start to form without a distinct pattern across the surface of the aluminum. The randomness in the portion nucleation sites is shown in Fig. 5.a.

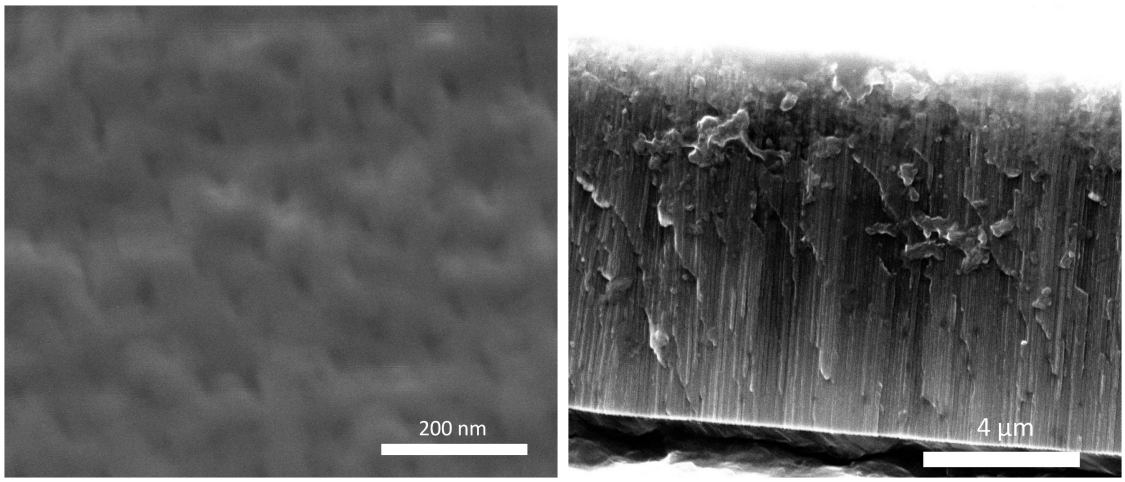

(a) Top view (b) Cross-sectional view

Fig. 5. AAO template after 1^{st} anodization.

The appearance of randomness in the location of the nanopores will continue for some distance into the aluminum film, however eventually the pores will align themselves due to the pore walls. As shown in Fig. 5.b, the distance until the nanopores become well ordered can be as long as 6 µm. According to Fig. 5.b, the total length of the nanopores after the first anodization is approximately 9.1 µm. These images indicate a definite need to remove the top of the anodized layer in order to obtain a well ordered nanoporous array.

The next step in the fabrication process is to dissolve the first layer of the AAO. This step is designed to dissolve the top of the first anodization, thereby removing the part of the AAO which was random after the first anodization. The dissolving step does not, however, need to remove the entire first anodization layer since the nanopores fabricated in the AAO template after the first anodization obtain regularity after approximately 6 µm, as discussed for the first anodization. The fact that entire first anodization layer was not completely removed can be seen in the slight abnormalities shown in the surface of the AAO template in subsequent steps. For in-

stance, the irregular spacing of certain nanopores in Fig. 1 shows that, although most of the irregular portion of the AAO fabricated during the first anodization was dissolved, a few of the original irregular nanopores from the first anodization remained. However, comparing Fig. 1 to Fig. 4, it is clear that the new parameters for the dissolving step allow for a more complete dissolving of the irregular portion of the nanopores fabricated during the first anodization.

After the dissolving step, the second anodization is used primarily as a means to grow the nanopores into long and regular nanopores. The growth of the nanopores during the second anodization uses the templated surface left after dissolving the first anodization to determine the location of the center of the nanopores. The templated surface left after the dissolving step can be seen in Fig. 6 by the ridges on the surface of the AAO template after the second anodization. The length of the nanopores is determined by the length of time used in the second anodization. Through experimentation, it was found that the length of the nanopores for AAO templates with a second anodization of 1 hour was approximately 10 μm. Alternatively, if the second anodization lasted for 2 hours, the length of the nanopores was approximately 15 μm. Therefore the growth of the nanopores shows a nonlinear increase in length during the second anodization. The reason for the nonlinear increase in depth is due to a decreasing rate of dissolution as the nanopores deepen. As the length of the nanopores increases, it becomes increasingly difficult to transport the dissolved ions away from the bottom of the nanopores, therefore causing the reduction in the rate of dissolution of the underlying aluminum substrate. However, it should also be noted that when the second anodization is allowed to continue for long periods of time, the entire aluminum substrate was completely dissolved, indicating that the rate of dissolution does not decrease to 0. The average nanopore diameter in Fig. 6.a is approximately 41 nm. Also, according to Fig. 6.b, the length of the nanopores

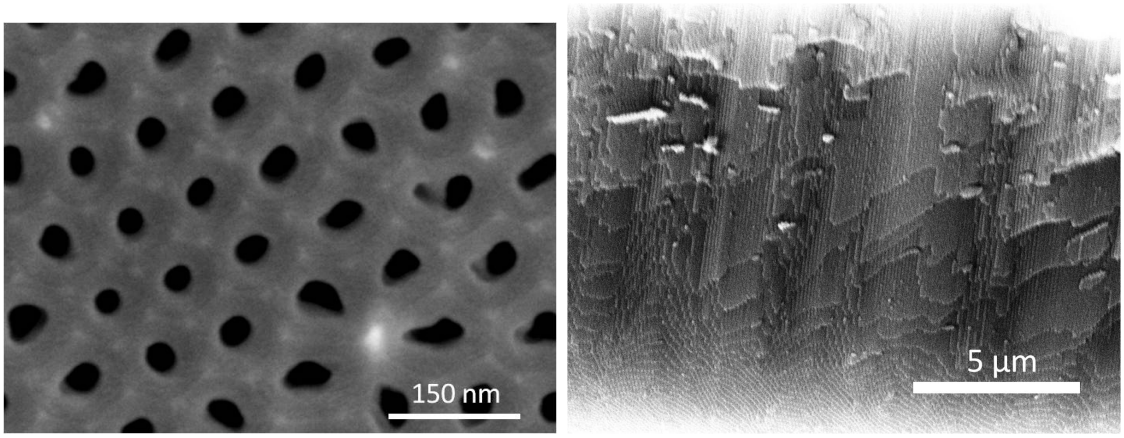

(a) Top View (b) Cross Section View

Fig. 6. AAO template after 2^{nd} anodization.

is approximately 13 µm. Therefore, the second anodization did not last the full two hours but was close.

After the second anodization, the nanopores should be fully formed. The remaining steps are designed to enlarge the pores. The pore widening procedure, as described previously, is comprised of five steps: 3 phosphoric acid baths and 2 heat treatments. The acid baths are designed to dissolve the nanopore walls in a controlled manner such that the pores become progressively larger. The heat treatments are used to strengthen the nanopores such that they will be able to withstand the pressure applied by the hydraulic jack to inject the liquid metal. For brevity, SEM micrographs after the first and second heat treatments are not shown. The effects of these heat treatments are shown in combination with the effects of the second pore widening and the finished AAO template, respectively. After the first pore widening procedure, the diameter of the nanopores widened from approximately 41 nm after the second anodization to approximately 48 nm as shown in Fig. 7.a. Due to the angle of the template with respect to the beam of the SEM, the length of the nanopores could not be determined from Fig. 7.b. However, as the pore widening process does

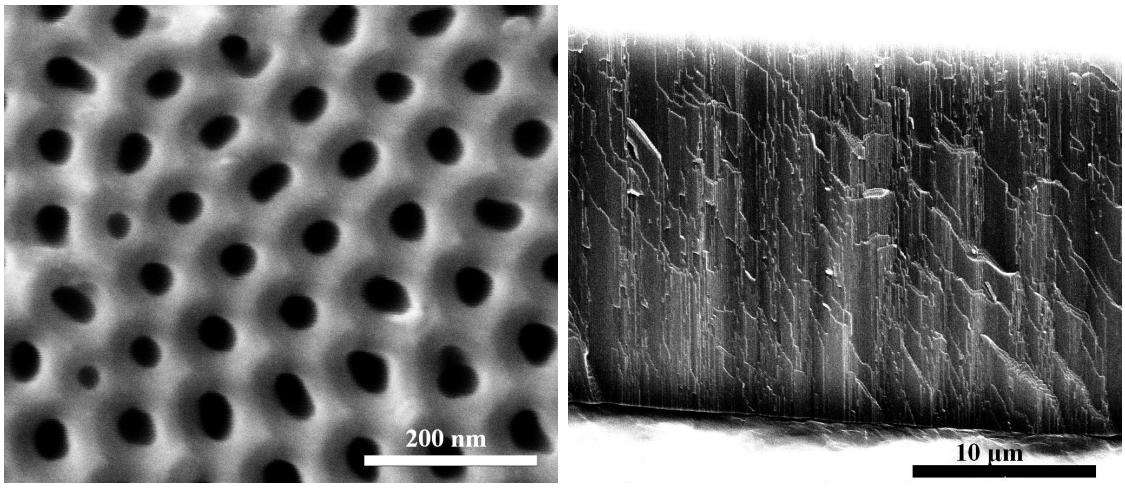

(a) Top view (b) Cross-sectional view

Fig. 7. AAO template after 1^{st} pore widening.

not anodize the aluminum substrate any further, it is expected that the nanopore length will not be changed by the pore widening (or the heat treatment) steps left in the AAO template fabrication procedure.

The heat treatments are designed to strengthen the AAO template nanopore walls by crystallizing the microstructure. The as-grown AAO exhibits a large amount of disorder and therefore the bonds between the atoms are relatively weak. The nanopore walls must therefore be strengthened due to the high load placed on the walls during the injection step of the mechanical pressure injection method to fabricate nanowires. In conjunction with the heat treatments, further pore widening steps are performed in order to widen the nanopores. By combining these two treatments together, the walls are strengthened while the nanopores continue to be fully formed. However, since the heat treatments strengthen the nanopore walls, the diameter of the nanopores does not significantly increase during the second and third pore widening steps. The top view of the AAO template after the second pore widening step is shown in Fig. 8.a. The diameter of the nanopores is approximately 52 nm. As

expected, the rate of pore widening has reduced after the first heat treatment due to the strengthening and ordering of the nanopore walls. The second pore widening lasted for 80 minutes and only enlarged the nanopore diameter by approximately 4 nm. In contrast, the first pore widening only lasted 15 minutes but resulted in a change of 7 nm in the average nanopore diameter. The reduction in pore widening rate is evident from the change in nanopore diameter from 52 nm to 55 nm, as shown in Fig. 8.b.

The third pore widening step finishes the AAO template fabrication procedure. The surface and cross section of the AAO template as shown in Figs. 1, 8.b, and 8.c are examples of the final results of the AAO template fabrication procedure. As with the cross-sectional view after the first pore widening, however, none of these images can be used to determine the exact length of the nanopores after completion of the AAO template fabrication due to the unknown angle of the cross-section with respect to the electron beam from the SEM. It can be concluded from Fig. 8.c, however, that the length of the nanopores is at least 11.5 μm, which agrees with the length of the nanopores as determined from Fig. 6 of 13 μm.

2. Fabrication of AAO Templates of Various Diameters

The fabrication of metallic nanowires with various diameters requires the fabrication of AAO templates of various nanopore diameters. Therefore, certain parameters of the AAO template fabrication procedure were modified. The primary parameters changed were the electrolyte and anodization voltage used during the anodization procedure, as shown in Table II. Another difference to the original AAO template fabrication procedure was the etching time and length of heat treatment. The rest of the fabrication procedure remained the same as previously described. The changes to the fabrication procedures of the AAO templates were in accordance with the

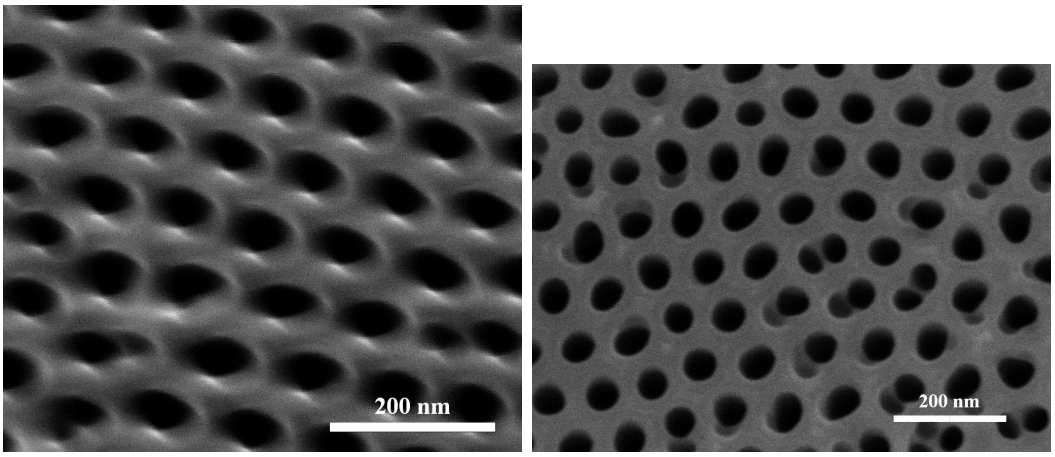

(a) Top view after 2^{nd} pore widening (b) Top view after 3^{rd} pore widening

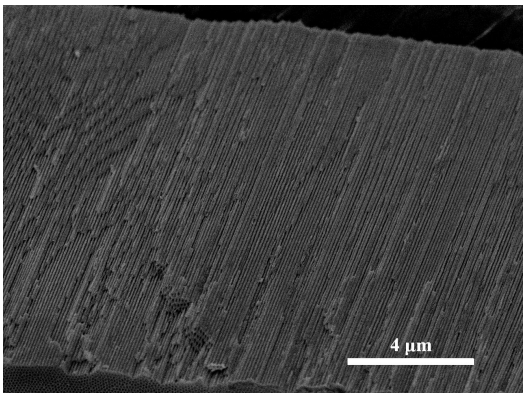

(c) Cross sectional view

Fig. 8. AAO template after 2^{nd} and 3^{rd} pore widening.

Table II. Anodization parameters for fabrication of various nanowire diameter

Pore diameter (nm)	*Electrolyte*	*Voltage*	*Etching Time (min)*	*Heat Treatment Time (hours)*
10	10vol%H_2SO_4	10	N/A	N/A
15	10vol%H_2SO_4	18	N/A	N/A
60	3vol%$C_2H_2O_4$	40	80	8
180	2vol%H_3PO_4	85	40	8
300	2vol%H_3PO_4	115	60	6

fabrication procedures as detailed in the literature [44, 45, 46, 47, 48].

The results of using the parameters in Table II for the fabrication of 15 nm nominal pore diameter AAO templates can be seen by examining Fig. 9.a. If it is assumed that the nanopores shown in the figure are circular, calculations using ImageJ [78] give an average pore diameter of 14.98 nm, indicating that the procedure utilized gives appropriate results. However, controlling the pore size for larger nanopore diameter AAO templates was much harder, as shown in Fig. 9.b. The AAO template shown in Fig. 9.b was fabricated using the parameters for the 180 nm pore diameter and gave a much wider range of diameters, from 105 nm to 175 nm. Clearly, it is more challenging to control the diameter of the larger nanopores than it is to control the diameter of smaller nanopores.

Once the AAO templates of the desired nanopore diameter were fabricated, the rest of the mechanical pressure injection method as described previously was followed. The variety in AAO template nanopore diameter thus allowed for the fabrication of InTl nanowires of various diameter.

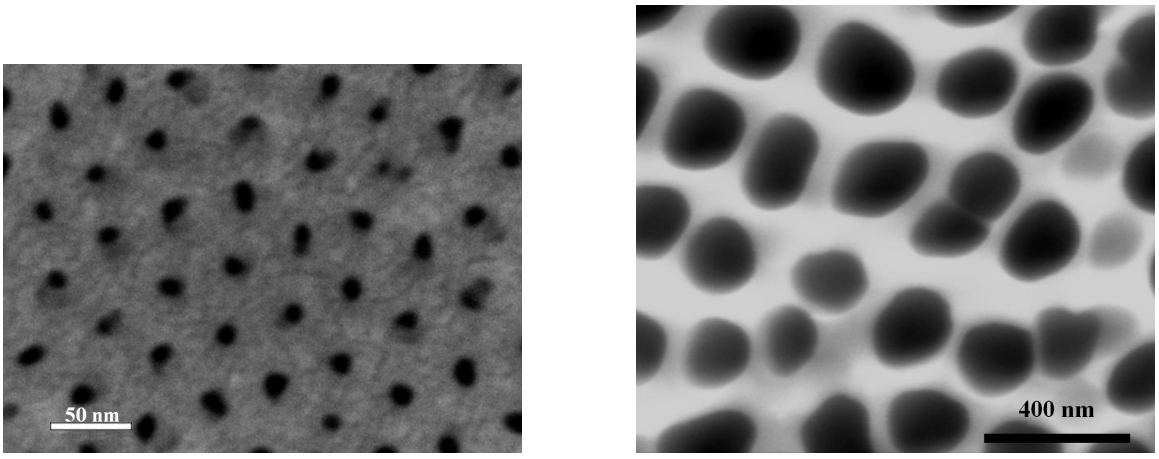

(a) 15 nm nominal diameter (b) 180 nm nominal diameter

Fig. 9. AAO templates with varying nominal nanopore diameter.

3. Electrospinning of Metallic Nanowires in Polymeric Nanofibers

In order to find a method by which metallic nanowires could be incorporated into other systems, it was decided to electrospin Sn nanowires into a silica nanofiber. The Sn nanowires were fabricated through the mechanical pressure injection method as described in Sect. A using AAO templates with a nominal nanopore diameter of 60 nm. The incorporation of metallic nanowires into polymeric nanofibers should enhance certain properties of silica nanofibers, specifically their electrical and thermal conduction properties. Using the electrospinning process previously described, Sn nanofibers were successfully electrospun into silica nanofibers, as shown in Fig. 10.a. Figure 10.b shows an Electron Diffraction Spectroscopy (EDS) result for the electrospun nanofiber. In Fig. 10.b, the carbon and copper peaks are due to the transmission electron microscope (TEM) grid on which the silica nanofiber are electrospun.

These results are the first to show coaxially aligned metallic nanowires in polymeric nanofibers. The ability to coaxially align metallic nanowires with polymeric nanofibers presents an entire new range of possible applications for such nanofibers.

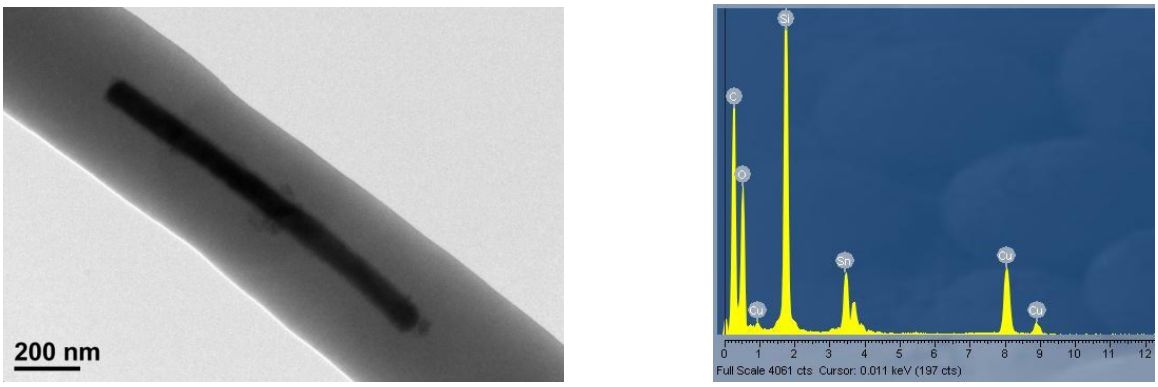

(a) TEM bright field image (b) EDS result

Fig. 10. Electrospun silica nanofiber with embedded tin nanowire.

It is expected that the incorporation of metallic nanowires into polymeric nanofibers will allow for the enhancement of such properties as the mechanical strength, thermal conductivity, and electrical conductivity of the nanofibers. Such a composite structure could also be used to protect metallic nanowires against oxidation or other environmental factors. Furthermore, the electrospinning of SMA nanowires into polymeric nanofibers will allow for the active motion of the nanofibers through the phase transformation of the SMA nanowires. However, as indicated previously, the phase transformation behavior of an SMA nanowire has not yet been investigated to determine whether a size effect exists on the phase transformation of the SMA nanowires and will therefore be investigated in Ch. III.

One preliminary characterization which can be performed using the fabricated silica/Sn nanofibers is to determine the electrical properties of these nanofibers. It was anticipated that the incorporation of metallic nanowires into polymeric nanofibers would enhance the thermal conductivity of the polymeric nanofibers. However, preliminary testing of these nanofibers has shown that the electrical conductivity of these nanofibers does not appreciably change with the addition of the nanowires. Several

ideas have been brought forth as to why the addition of nanowires did not increase the electrical conductivity of the nanofibers. First, re-examination of the nanowires showed a thin oxide layer. The oxide layer formed on the surface of the nanowire will prevent the flow of electricity from the less conductive silica to the more conductive Sn nanowires.

A second idea which has been brought forth is related to the dispersion of the nanowires. Dispersion can be thought of as the degree to which a solute (the nanowires) is distributed throughout a solvent (the silica). In order to achieve an appreciable gain in electrical conductivity, the Sn nanowires would need to be well dispersed throughout the nanofibers. However, as shown in Fig. 11, the Sn nanowires tend to bundle together. Furthermore, the Sn nanowires would need to be close enough to each other in order to allow the formation of a conductive path. Figure 11 shows that an insufficient number of nanowires could be found close to each other to form a conductive path through the nanofibers. Thus, the dispersion and the amount of Sn nanowires are also partly responsible for the lack of appreciable change in electrical conductivity of the silica nanofibers.

C. Conclusion

This chapter has presented the mechanical pressure injection method, methods to modify the mechanical pressure injection method in order to achieve nanowires of various diameter, and a method to use metallic nanowires within a different system. The mechanical pressure injection method can be split into three parts: the fabrication of an AAO template, the injection of molten metal into the AAO template, and the release of the nanowires from the AAO template. A step by step study of the fabrication of the AAO templates has been performed and the results show

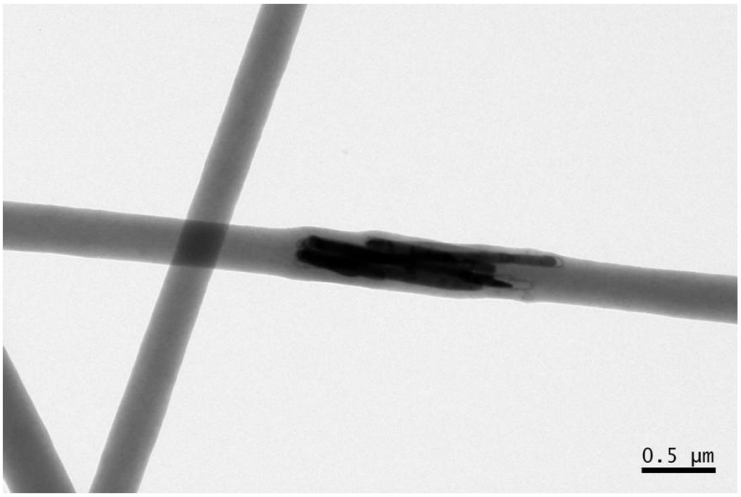

Fig. 11. Bundle of Sn nanowires within a silica nanofiber.

that, by dissolving the first anodization for longer than initially required, regular and well formed AAO nanopores formed on top of an aluminum substrate. The steps to obtain the formation of the AAO templates are: first anodization, dissolve, second anodization, pore widen, heat treat, pore widen, heat treat, and pore widen again. These steps were summarized in Table I. Analysis of each step in the AAO template fabrication procedure showed what parameters could be changed in order to obtain nanoporous AAO templates of various diameters. Specifically, prior to the widening steps, the nanopores had a diameter of 47.5 nm. Also, since the nanopores are formed due to anodization, the parameters of the anodization, such as the voltage and the electrolyte, were changed to fabricate AAO templates with nanopores of different diameters. Results showed that as the target size of the nanopore diameter increased, the range of diameters of the fabricated nanopores also increased.

This chapter also presented a method by which metallic nanowires can be incorporated into another structure. Specifically, metallic nanowires have been embedded into polymeric nanofibers by electrospinning Tin (Sn) nanowires into silica nanofibers. The fabrication of coaxially aligned metallic nanowires into polymeric nanofibers has

been successfully accomplished for the first time in this study. The incorporation of metallic nanowires into polymeric nanofibers was expected to increase a range of properties, including the electrical conductivity of these nanofibers. However, preliminary results indicate no appreciable change in electrical conductivity. Possible reasons for the lack of appreciable change in electrical conductivity of the silica/Sn composite nanofibers are the formation of an oxide layer on the Sn nanowires, as well as the poor dispersion and insufficient quantity of the Sn nanowires throughout the silica nanofibers. The ability to coaxially align metallic nanowires in polymeric nanofibers allows for a number of new applications for such a composite system. One interesting possibility that such a system allows is for active change in the shape of the nanofiber through the embedding of SMA nanowires into the polymeric nanofibers. However, prior to embedding SMA nanowires into polymeric nanofibers, the phase transformation properties of SMA nanowires must be known in order to know if the SMA nanowires will cause any motion in the nanofibers.

CHAPTER III

SMA NANOWIRES

A brief introduction to Shape Memory Alloys (SMAs) was given in Ch. I. Additionally, Ch. I reviewed a number of works which have tried to illuminate the nanoscale behavior of SMAs. However, the works reviewed from the literature only address the phase transformation of SMAs in the shape of nanograins, nanocrystals, and thin films attached to a substrate. To the best of the author's knowledge, the following study presents the first systematic investigation of size dependence on the phase transformation for any kind of SMA nanowire. Nanowires are different than the other systems studied in the literature due to the single long axis, as opposed to nanograins and nanocrystals, which are equi-axed, or thin films, which have two long axes.

A. Experimental Procedures

The fabrication of SMA nanowires using the mechanical pressure injection method as described in Sec. A of Ch. II requires the use an SMA with a low melting temperature. The constraint that the SMA have a low melting temperature is satisfied through the use of an Indium-Thallium (InTl) alloy. As mentioned in the introduction, InTl alloys exhibit a reversible martensitic phase transformation for Thallium concentrations between 18at% and 30at%. Using a film of bulk InTl, fabricated as described below, InTl nanowires are fabricated using the mechanical pressure injection method. For this study it is necessary to investigate SMA nanowires of multiple diameters and, by fabricating AAO templates of various diameters as described in Sec. 2 of Ch. II, InTl nanowires of various diameters were fabricated using the mechanical pressure injection method.

1. Fabrication of the Bulk InTl Alloy

An Indium ingot (Alfa Aesar, 99.999% metals basis) and Thallium granules (Alfa Aesar, 99.999% metals basis) were mixed in appropriate atomic percentages by measuring the mass using an electronic balance and converting the mass of each elemental precursor into atomic percentages. The measured amounts of the elemental precursors were sealed in an evacuated quartz tube and melted in a conventional muffle furnace at 400 °C for 24 hours. The resulting InTl ingot was subsequently homogenized at 125 °C for 48 hours. The InTl ingot was removed from the quartz tube by carefully breaking the tube. For verification of the anticipated crystallographic results from [58, 60], X-Ray Diffraction (XRD) (Bruker D8 X-Ray Diffractor) studies were performed. In order to select a composition that is martensitic at room temperature, two bulk alloys of InTl, In-21at%Tl and In-26at%Tl, were fabricated. It is desired to have the SMA be martensitic at room temperature because a size effect on the phase transformation of an SMA nanowire would lower the phase transformation temperature. Therefore, if it is observed that at room temperature the nanowires have an austenitic crystal structure, then it would be clear that a size effect on the phase transformation of SMA nanowires exists. Furthermore, the available equipment for crystallographic identification studies can be heated instead of cooled and therefore, in order to observe a phase transformation upon heating, the bulk material must be in the martensitic phase at room temperature.

2. Characterization of InTl Nanowires

The InTl nanowires were characterized through the use of a Scanning Electron Microscope (SEM) (FEI Quanta 600 FE-SEM equipped with a Oxford EDS system with X-ray mapping and digital imaging) and a Transmission Electron Microscope (TEM)

(JOEL JEM-2010 equipped with an in-situ heating stage). The SEM was used in order to verify the diameter and length of the fabricated nanowires. Electron Diffraction Spectroscopy (EDS) was used to verify the composition of the nanowires. The TEM was used to verify nanowire diameter and to determine the crystal structure of the nanowires. The crystal structure of the nanowires was determined by analyzing the selected area electron diffraction (SAED) patterns at multiple locations along larger nanowires and for groups of nanowires with similar dimensions. Samples for the SEM and TEM of the nanowires were prepared by placing a drop of ultrasonicated ethanol bath containing the nanowires onto a copper TEM grid and allowing the ethanol to evaporate, leaving the nanowires on the TEM grid. Sonicating the vials containing the nanowires and ethanol dispersed the nanowires throughout the ethanol bath. As with the Sn nanowires, however, sonicating the vials containing the ethanol bath and nanowires resulted in breaking of the nanowires into smaller nanowires. For the smaller diameter nanowires, the vials were instead shaken manually to disperse the nanowires in order to minimize damage to the nanowires.

B. Results

The fabricated bulk In-21at%Tl and In-26at%Tl alloys were first analyzed to study what can be learned from these bulk materials. Specifically of interest was the phase of the material at room temperature and the phase transformation temperature, which are important when choosin the alloy from which to make the nanowires. The second portion of the results section is dedicated to characterizing the fabricated InTl nanowires, with emphasis on their phase transformation behavior.

1. Bulk In-21at%Tl and In-26at%Tl Alloys

The phase transformation behavior of the bulk alloy is of critical importance because the purpose of the current study is to determine whether a size effect on the phase transformation exists in the associated nanowires. As discussed in Ch. I, the phase transformation of Indium-Thallium alloys goes from an FCC austenitic phase to an FCT martensitic phase. One method often used to determine the crystal structure of a material is to use XRD. The results of the XRD scans at room temperature on the In-21at%Tl and In-26at%Tl bulk alloys are shown in Figs. 12.a and 12.b, respectively.

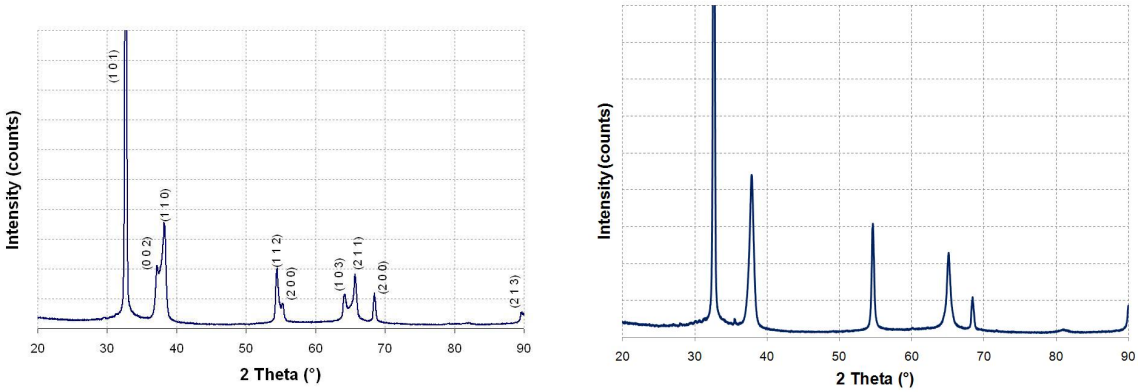

(a) In-21at%Tl (b) In-26at%Tl

Fig. 12. XRD patterns at room temperature of In-21at%Tl and In-26at%Tl bulk alloys.

The XRD patterns shown in Fig. 12 show a difference in the crystal structure due to the differences in the location of the 2θ peaks. After indexing these peaks, it was determined the In-21at%Tl alloy had an FCT crystal structure. Therefore, the In-21at%Tl alloy was in the martensitic phase at room temperature. On the other hand, the In-26at%Tl alloy had an FCC austenitic crystal structure at room temperature. These results match the results as given by Schumann [60]. According to the literature, a size effect on the phase transformation will decrease the phase

transformation temperature [15]. Since In-21at%Tl was in the martensitic phase at room temperature, the phase transformation temperature of In-21at%Tl was above room temperature. Therefore, a simple way to determine the existence of a size effect on the phase transformation would be to determine the crystal structure of In-21at%Tl at room temperature for a variety of sizes. It was thus decided to further investigate In-21at%Tl. Also, In-21at%Tl has a relatively low melting temperature ($\approx$ 160 °C) which is ideal for the fabrication of nanowires using the mechanical pressure injection method.

The next step in the characterization of the In-21at%Tl bulk alloy was to determine the phase transformation temperature. The phase transformation temperature was determined by heating and cooling the In-21at%Tl bulk alloy in the XRD chamber. The results of various scans at different temperatures are shown in Fig. 13. The first XRD pattern is taken at 30 °C and then the sample is heated as indicated to the right side of Fig. 13. The peaks of the XRD patterns change as the sample is heated from 50 °C to 65 °C. The change in peak locations indicates that the reverse transformation from martensite to austenite occurs between 50 °C and 65 °C. As mentioned in Ch. I, the hysteresis between the forward and reverse transformation temperatures is 1-2 degrees [59]. Thus, by cooling the sample in smaller increments, it is possible to more accurately determine the approximate transformation temperature. Cooling the sample from 65 °C to 50 °C was done from steps t_3 to t_6, corresponding to cooling in 5 °C increments. The FCT martensitic crystal structure is recovered as the sample was cooled from 55 °C to 50 °C. Thus the phase transformation temperature for the In-21at%Tl bulk alloy is between 50 °C and 55 °C, which is in agreement with Jaglinski *et al.* [58].

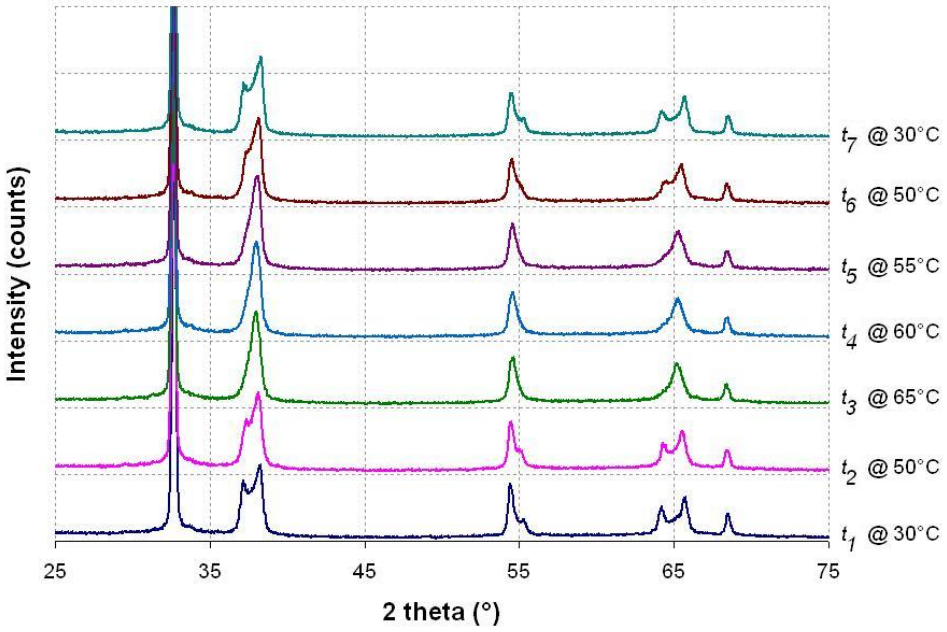

Fig. 13. XRD patterns of In-21at%Tl bulk at various temperatures.

2. In-21at%Tl Nanowires

As was discussed in Ch. I, it has been experimentally observed that for SMA nanograins of Nickel Titanium, there is a critical diameter of approximately 50 nm below which the martensitic phase transformation is inhibited [15]. However, no previous experimental work has been performed on SMA nanowires in order to determine if a size effect on the phase transformation exists. Therefore, the following presents the first systematic study on the existence of a size effect for an SMA nanowire.

Prior to verification of any size effect on the phase transformation temperature, it was necessary to verify that the nanowires fabricated had the same composition as the bulk material. The first nanowires fabricated had a diameter of 60 nm and samples of these nanowires were taken to the SEM, both in the AAO templates and after being released. As shown in Fig. 14.a, the In-21at%Tl nanowires were

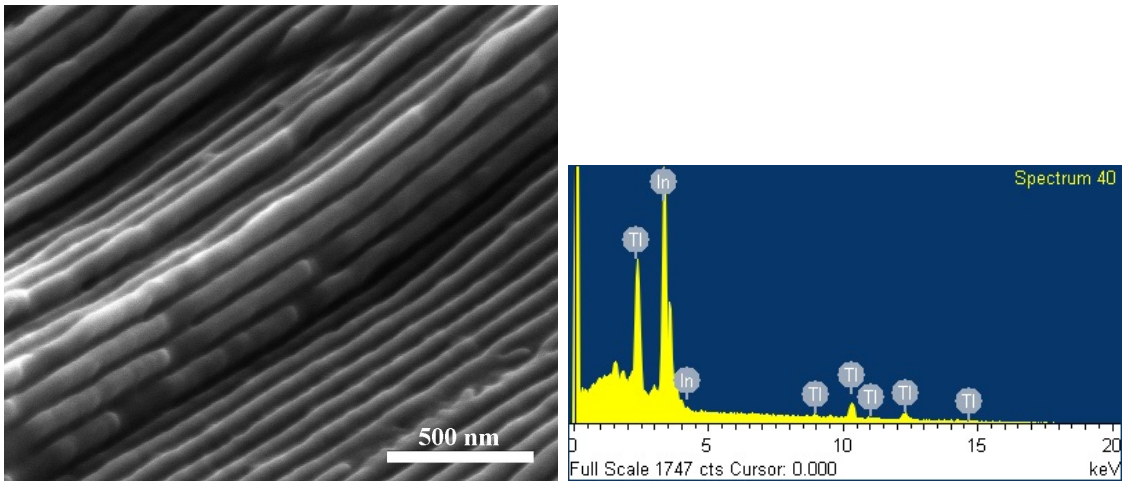

(a) SEM micrograph of AAO template cross-section with embedded In-21at%Tl nanowires

(b) EDS of a nanowire

Fig. 14. In-21at%Tl nanowires in cross-section of an AAO template and EDS of a nanowire.

grown throughout the cross-section of the AAO templates. In order to determine the composition of these nanowires, a series of EDS studies were performed on various nanowires after they had been released from the AAO templates. Figure 14.b shows one such study. The composition of various nanowires is shown in Table III. These results indicate that the mechanical pressure injection method fabricates nanowires of the same chemical composition as the film placed above the AAO template.

Since the nanowires produced provided the same chemical composition as the bulk material, it was determined that the analysis of the size effect on the phase transformation of In-21at%Tl nanowires should start with the largest diameter nanowire possible. Comparison with other studies indicates that at the largest size, the phase transformation behavior should be most like the bulk material [15]. As mentioned in Sec. 2 of Ch. II, the fabricated AAO templates had a range of nanopore diameter on each template. Furthermore, it was shown that AAO templates with a larger target

Table III. Composition of various 60nm diameter nanowires. Target nanowire composition is 79at%In-21at%Tl

Element	*Nanowire 1*	*Nanowire 2*	*Nanowire 3*
In	78.95at%	78.88at%	79.87at%
Tl	21.05at%	21.12at%	20.13at%

nanopore diameter had a wider range of fabricated nanopore diameters than AAO templates with a smaller target nanopore diameter. With the variation of AAO template nanopore diameter in mind, it should not surprise the reader that the following results are for nanowires with different diameters than the target nanopore diameter of the AAO templates from which they are fabricated.

In a certain sample of nanowires which should have had a nominal diameter of 300 nm, it was observed that a nanowire of approximately 650 nm was fabricated. The reason why the 650 nm diameter nanowire was fabricated was due to the merging of two or more nanopores. Although the surface and cross section of a 300 nm nanopore diameter AAO template has not been shown, looking at Figs. 1.a and 9 indicates that the merging of two or more nanopores to make a nanopore with a larger diameter will occur. Using Selected Area Electron Diffraction (SAED) as shown in Fig. 15, the 650 nm diameter nanowire was indexed to an FCT crystal structure at room temperature, which matches the cystal structure of the bulk alloy at room temperature, as expected. By comparison with results from previous studies, one would not expect to observe any noticeable size effect until the diameter is significantly reduced. Similar results were also found for nanowires with diameters of 260 and 180 nm. Using dark field imaging in the TEM, Fig. 16 shows that the twin structure typical of SMAs is present

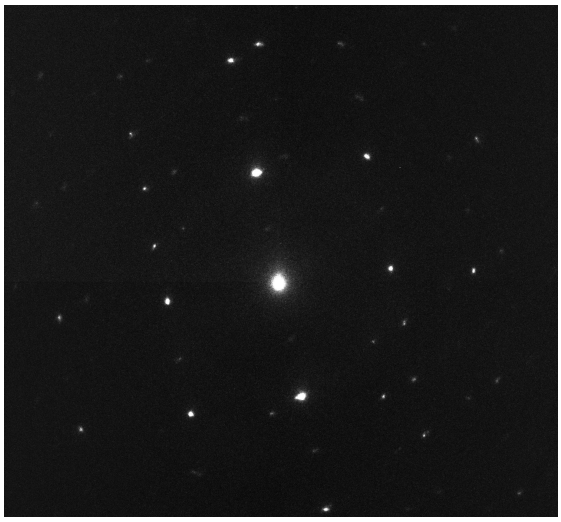

Fig. 15. SAED pattern of 650 diameter In-21at%Tl nanowire at room temperature.

in the 260 nm diameter nanowire. The pattern of twin boundaries found in Fig. 16 was found throughout the length of the nanowires, however due to the focus, only a portion of the nanowire shows the twin boundaries. Similar patterns were found in nanowires with a diameter of 180 nm. However, for brevity, the micrographs corresponding to the 180 nm nanowires have been omitted from this thesis. The results for the 260 nm and 180 nm In-21at%Tl nanowires matched the expectation that no size effect on the phase transformation temperature would be observed at these diameters.

The next step taken was to determine whether there was any effect on the phase transformation temperature for nanowires with a diameter of 60 nm. After analyzing the available literature, a size effect on the transformation temperature may start to be observed around a diameter of 60-70 nm [15]. The existence of a size effect on the phase transformation would be most clearly observed through a depression of the transformation temperature. Since the transformation temperature for the bulk alloy was experimentally determined to be between 50 °C and 55 °C, one clear

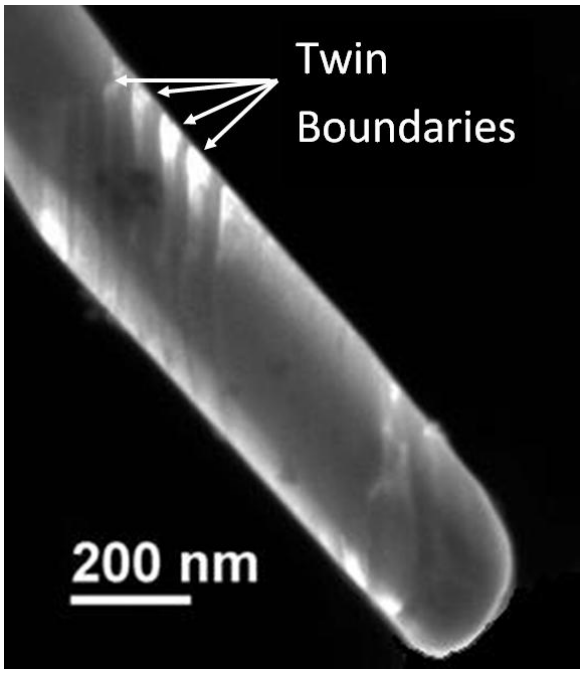

Fig. 16. TEM dark field micrograph of In-21at%Tl nanowire at room temperature with a diameter of 260 nm. The lines indicate twin boundaries.

indication of a size effect would be for the nanowires to be in the austenitic state at room temperature. If the size effect has lowered the transformation temperature of the nanowires, then the nanowires would have an FCC crystal structure at room temperature.

The nanowires fabricated to test the above hypothesis actually tended to be slightly larger than anticipated for an AAO template with a nominal pore diameter of 60 nm. As shown in Fig. 17.a, the fabricated nanowires had an average diameter close to 75 nm. It is believed that the difference between the anticipated and actual nanowire diameter was caused by slight differences in the fabrication procedure for the utilized AAO template. Nevertheless, since the material system under consideration is different than the material systems studied in the literature, one could still expect to start seeing a shift in the transformation temperature at the 75 nm diameter scale.

However, as shown in Fig. 18.a, a 70 nm diameter In-21at%Tl nanowire still retained the twin boundaries indicating the martensitic phase at room temperature. Upon heating to 100 °C, the twin structure disappeared, as shown in Fig. 18.b. In order to determine what had happened, the SAED patterns for the nanowires shown in Fig. 17.a were analyzed at room temperature and at 100 °C. The reason that it is easier to determine the crystal structure of a larger sample is because the larger sample allows for more nanowires to be involved and thus produces a more reliable pattern. The SAED patterns for the 70 nm diameter In-21at%Tl nanowires at room temperature and at 100 °C are shown in Figs. 17.b and 17.c, respectively. These patterns indicate that at room temperature, the nanowires had an FCT crystal structure. However, the nanowires had an FCC crystal structure at 100 °C. It should be noted that upon cooling, the nanowires regained their twinned microstructure and correspondingly, their FCT crystal structure. These results indicate that no size effect is noticeable for the 75 nm diameter nanowires.

Since no size effect on the phase transformation was yet found, it was therefore necessary to fabricate nanowires of even smaller diameters. Therefore, nanowires of 15 nm diameter were fabricated. One such nanowire is shown in Fig. 19.a. The nanowire shown in Fig. 19.a was fabricated as part of a large sample of similar diameter nanowires and therefore a different section of the 15 nm diameter nanowire sample was observed using SAED in order to determine the crystal structure. The sample area from which the SAED patterns were taken is shown in Fig. 19.b. The associated SAED patterns at room temperature and after heating to 100 °C are shown in Figs. 19.c and 19.d, respectively. The SAED pattern after cooling back to room temperature is shown in Fig. 19.e. These SAED patterns indicate that at room temperature, the 15 nm In-21at%Tl nanowires had an FCT crystal structure, but upon heating they transformed to an FCC crystal structure.

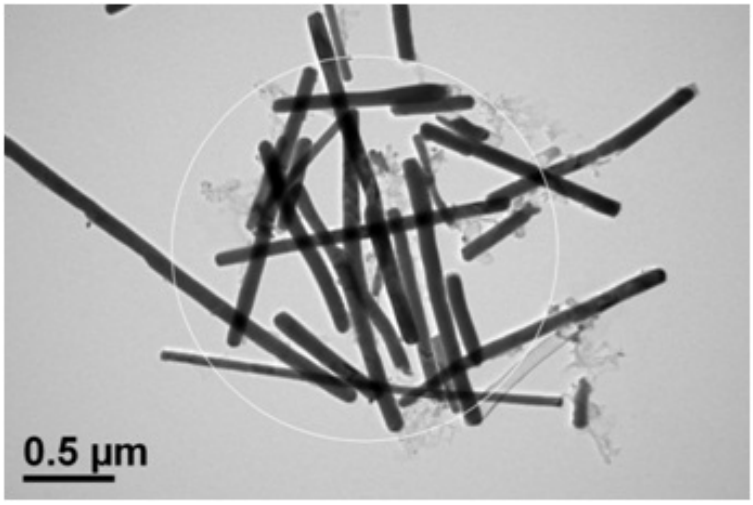

(a) TEM micrograph of nanowire group (circled)

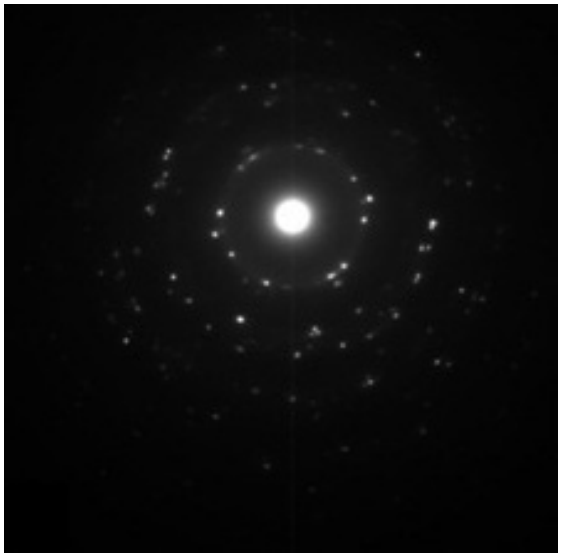

(b) SAED pattern at room temperature

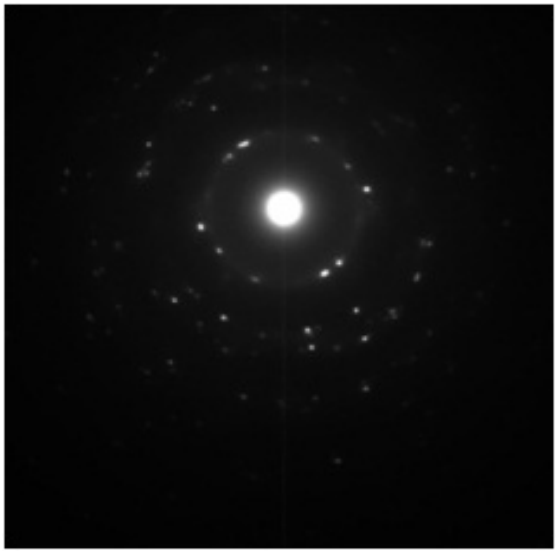

(c) SAED pattern at 100 °C

Fig. 17. Group of In-21at%Tl nanowires with an average diameter of 75 nm.

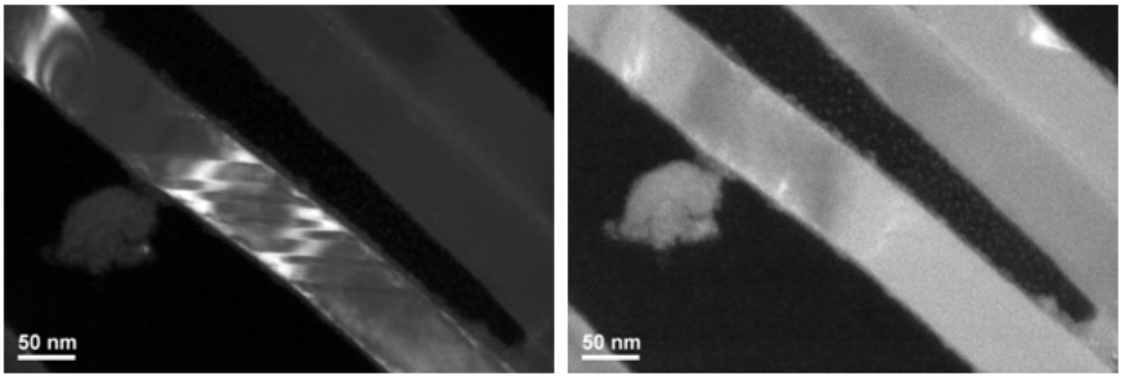

(a) Dark field micrograph at room temperature (b) Dark field micrograph at 100 °C

Fig. 18. In-21at%Tl nanowire with a diameter of 70 nm.

By slightly modifying the AAO anodization parameters, it was found that AAO templates with an average nanopore diameter of approximately 10 nm could be fabricated. Using these templates, In-21at%Tl nanowires with an average diameter of 10 nm were fabricated. As shown in Fig. 20.a, these nanowires were not as regular as the nanowires fabricated in the larger templates. These nanowires, however, still demonstrated a phase transformation upon heating, as shown in Figs. 20.b and 20.c. It can therefore be concluded that no size effect on the phase transformation of In-21at%Tl nanowires exists down to a diameter of at least 10 nm.

C. Conclusion

Through an experimental study, it has been found that a size effect on the phase transformation of In-21at%Tl nanowires could not be detected for nanowires ranging in diameter down to 10 nm. The result obtained through the study presented is in direct contrast to other studies on various SMA nanostructures such as nanograins, nanocrystals, and thin films, which exhibit a limiting size below which the phase transformation is inhibited. The current study has fabricated and characterized the

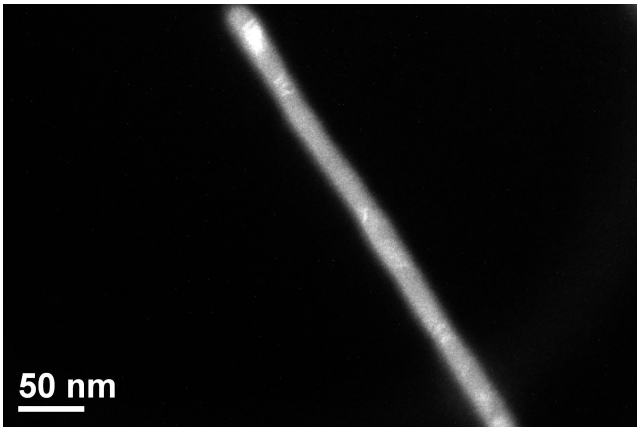

(a) TEM dark field of single nanowire at room temperature

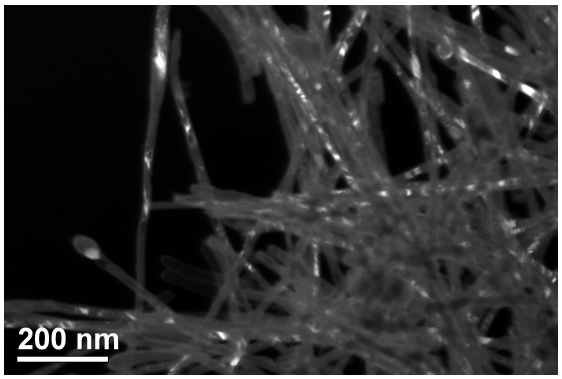

(b) TEM dark field micrograph at room temperature

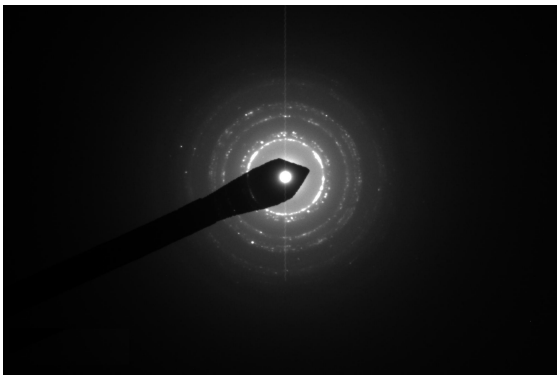

(c) Initial SAED at room temperature

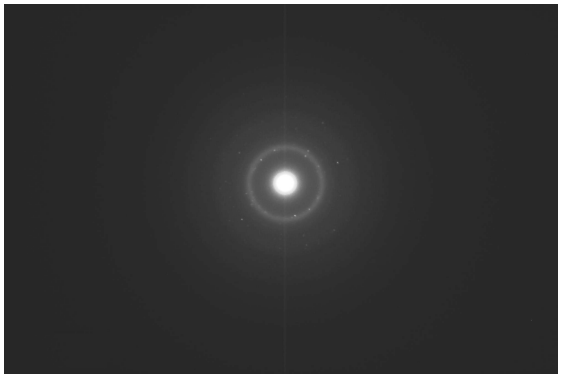

(d) SAED at 100 °C

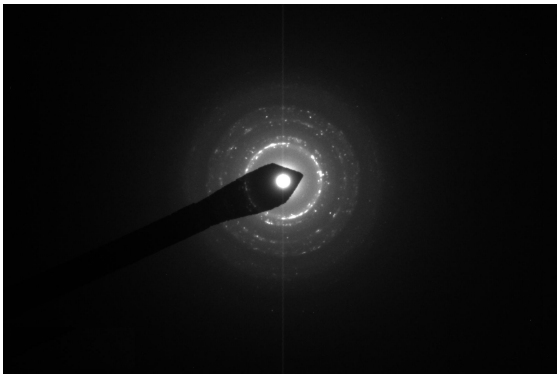

(e) SAED after cooling to room temperature

Fig. 19. Group of In-21at%Tl nanowires with a diameter of 15 nm.

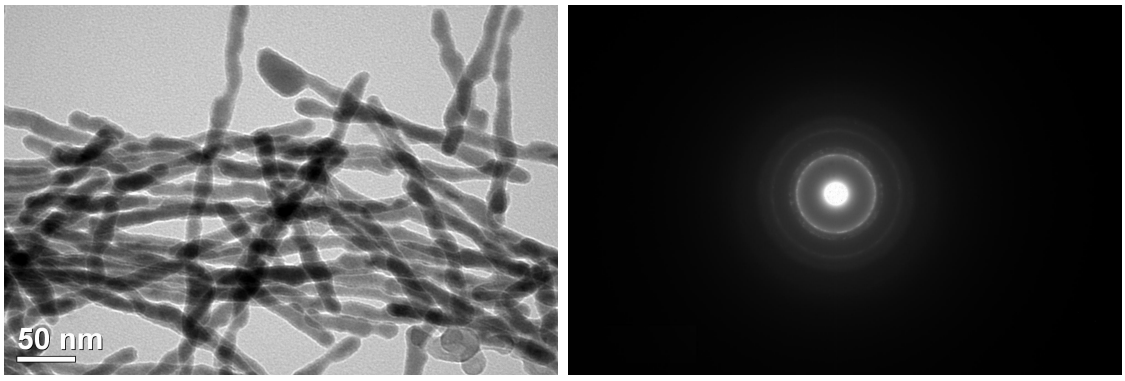

(a) TEM bright field micrograph at room temperature

(b) SAED at room temperature

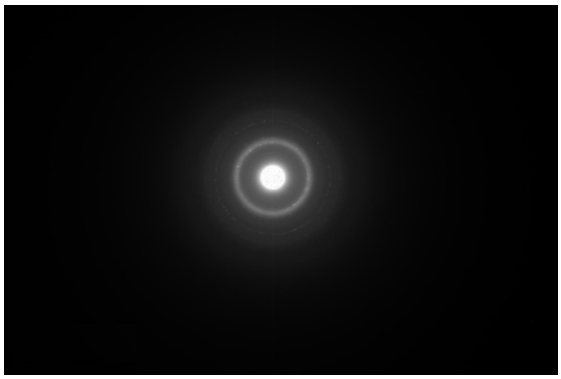

(c) SAED at 100 °C

Fig. 20. TEM and SAED results for 10 nm diameter In-21at%Tl nanowires.

phase transformation of a number of nanowires ranging in diameter from 650 nm to 10 nm. All of the characterized nanowires exhibited a reversible phase transformation from an FCT martensitic phase to an FCC austenitic phase.

The difference between the expected results and the results obtained experimentally could be due to a variety of factors, including the difference in material composition, the difference in dimensionality of the nanostructure, or the difference in constraints. The difference in material composition, however, should not significantly affect the expected results. As mentioned in Ch. I, a size effect has been found for various different compositions. Although the change in composition does affect the size at which a size effect is found, all the available literature on the size effect on the phase transformation of SMA nanostructures indicates a critical size below which the phase transformation temperature is either decreased or the phase transformation is completely suppressed. Therefore, it is expected that the difference in material composition is not the cause of the difference between the expected results and the results obtained experimentally.

On the other hand, the differences in dimensionality and constraints between this study and the studies performed in the literature are likely to have a large effect on the results. As mentioned previously, the studies on SMA nanostructures available in the literature are all for nanograins, nanocrystals, and thin films. However no other studies are available discussing the existence of a size effect for SMA nanowires. As mentioned in Ch. I, there have also been studies using molecular dynamics (MD) which show that unconstrained nanowires of certain metals exhibit a phase transformation when reduced to the nanoscale. Therefore, the difference between unconstrained nanowires and other shapes of nanostructures still needs to be investigated. Chapter IV will present such a study on the difference between the behavior of unconstrained nanostructures, specifically nanospheres, nanowires, and thin

films. However, as the MD studies discussed are all for unconstrained nanostructures, it will be informative to determine if the imposition of a constraint causes a change in the transformation behavior of nanostructures which otherwise transform at the nanostructure. Therefore, in order to determine if the imposition of a constraint causes the change in the behavior of the nanostructures, Ch. IV will also apply constraints on the transforming nanostructures. The unconstrained MD simulations will be most closely related to the free nanowires discussed in this chapter, where as the constrained MD simulations will be similar to the constrained nanograins and thin films found in the literature.

CHAPTER IV

MOLECULAR DYNAMICS SIMULATIONS OF NANOSTRUCTURES

The results found through the experimental study of SMA nanowires did not exhibit a size effect on the phase transformation, which is contrary to what would be expected based the available literature on SMA nanostructures. As mentioned previously, it has been experimentally shown that SMA nanograins and nanocrystals have a critical size below which their phase transformation is inhibited. One primary difference between the studies performed in the literature and this study, other than the composition, is the fact that this study analyzed the phase transformation of unconstrained SMA nanowires. Nanowires can be thought of as 1-D structures, where as nanograins and nanocrystals can be considered 0-D (or 3-D) structures. In order to investigate whether the dimensional difference could be the cause for the difference in resulting behavior, a parametric study using Molecular Dynamics (MD) was performed. Simulations using MD were also performed to determine if the difference between the expected and observed results are due to the difference in the constraints on the nanostructures. This chapter starts with a description of the MD simulation process, followed by a brief description of the interatomic force field used. Then the simulations performed both as precursors to and as part of the parametric study will be presented. Finally, the constraint effect will be discussed.

A. Molecular Dynamics

Molecular Dynamics or more generally molecular mechanics treats every atom as a point mass, and interactions between them are described through a force field. A force field is a set of parameters describing the interactions between the atoms which

are obtained either using experiments or *ab-initio* calculations [79] and is interpreted as a non-linear spring-type interaction. The equations of motion are setup for all the atoms using Newton's laws and the behavior of the atomistic system is then described by the solution to the equations of motion. Molecular mechanics facilitates the simulation of large numbers of atoms compared to quantum mechanical models and allows the behavior of up to a billion atoms to be computed. As previously mentioned, molecular mechanics can be further subdivided into molecular statics and MD. Since the simulations to be performed are time and temperature dependent, MD will be used.

1. Modified Embedded Atom Method

A variety of force fields have been parameterized for use in MD simulations. One particularly widespread force field is called the Embedded Atom Method (EAM), originally developed by Daw and Baskes [80, 73]. The EAM is a semiempirical, many-atom force field which has been used to compute the total energy of metallic systems. One problem with the EAM is that it does not account for angularly-dependent terms. The Modified Embedded Atom Method (MEAM) adds angularly-dependent terms, as well as compensates for certain other difficiencies in the original EAM [81]. It follows the same concepts as the EAM, while also including angle-dependent interaction terms using a multipole expansion. Since the crystal structure of a shape memory alloy changes, it is therefore important to be able to account for the change in bond angles.

The total energy for the MEAM can be written as a summation of the contributions from all the atoms. The total energy can be written as

$$E = \sum_i \left\{ F_i(\bar{\rho}_i) + \frac{1}{2} \sum_{j \neq i} \phi_{ij}(R_{ij}) \right\} \tag{4.1}$$

The first term of Eq. 4.1 is the embedding function of atom i into the background electron density $\bar{\rho}_i$. The background electron density is given by a linear superposition of spherically averaged electron densities augmented by the angular dependence. The second term in Eq. 4.1 is the pair potential between the i^{th} and j^{th} atoms with a separation of R_{ij}.

The parameterization process for an MD force field is not trivial in general due to the complexities of obtaining accurate inputs. In order to find the parameters for the MEAM force field, the sublimation energy, equilibrium lattice constants, bulk modulus, two shear constants, two structural energy differences, and the vacancy formation energy must be known. These inputs have been used to identify the 11 parameters for the MEAM force field for certain metals [82].

2. Numerical Integration

The total energy of the complete atomistic system, incorporating contributions from all atoms, is a function of positional coordinates of atoms, represented as

$$E = E(\mathbf{r}^{(1)}, \mathbf{r}^{(2)}, \mathbf{r}^{(3)} \ldots \mathbf{r}^{(N)}) \tag{4.2}$$

The expression for the potential energy is utilized to evaluate the total force on each atom

$$\mathbf{F}^{(i)} = -\nabla_{\mathbf{r}^{(i)}} E = F(\mathbf{r}^{(1)}, \mathbf{r}^{(2)}, \mathbf{r}^{(3)} \ldots \mathbf{r}^{(N)}) \qquad i = 1, 2, \ldots, N \tag{4.3}$$

Given the coordinates of the atoms, both the total energy as well as the force on individual atoms can be evaluated. The acceleration of an atom is evaluated by

Newton's law as:

$$\mathbf{a}^i = \ddot{\mathbf{r}}^i = \frac{\mathbf{F}^i}{m^i} \tag{4.4}$$

where m^i is the mass of the i^{th} atom. These are a set of $3N$ second order ordinary differential equations and are integrated in time using the velocity-Verlet integration algorithm [83] given as follows:

At a given time instant t, represented by the n^{th} time step of uniform duration h such that $t = nh$, the velocity and accelerations can be approximated using the central difference scheme as:

$$\mathbf{v}_n^i = \dot{\mathbf{r}}_n^i \approx \frac{1}{2h}\left(\mathbf{r}_{n+1}^i - \mathbf{r}_{n-1}^i\right) \tag{4.5}$$

$$\mathbf{a}_n^i = \ddot{\mathbf{r}}^i = \frac{\mathbf{F}_n^i}{m^i} \approx \frac{1}{h^2}\left(\mathbf{r}_{n+1}^i - 2\mathbf{r}_n^i + \mathbf{r}_{n-1}^i\right) \tag{4.6}$$

Treating the approximations as equalities, they can be rearranged to give:

$$\mathbf{r}_{n+1}^i = \mathbf{r}_n^i + h\mathbf{v}_n^i + \frac{h^2}{2}\frac{\mathbf{F}_n^i}{m^i} \tag{4.7}$$

$$\mathbf{v}_{n+1}^i = \mathbf{v}_n^i + \frac{h}{2}\left(\frac{\mathbf{F}_{n+1}^i}{m^i} + \frac{\mathbf{F}_n^i}{m^i}\right) \tag{4.8}$$

At the beginning of the MD simulation, the positions and velocities of all the atoms are known (initial conditions: $\mathbf{r}_0^i$, $\mathbf{v}_0^i$, $i = 1 \ldots N$) and the information of positions ($\mathbf{r}_0^i$) allows the evaluation of acceleration for all atoms using Eq. 4.4 ($\mathbf{a}_0^i$, $i = 1 \ldots N$). The positions of atoms at the next time step ($\mathbf{r}_1^i$) are evaluated using Eq. 4.7. With the new positions of atoms, Eq. 4.4 is used to calculate accelerations on all the atoms ($\mathbf{a}_1^i$) and Eq. 4.8 gives the velocities ($\mathbf{v}_1^i$) of all atoms at the next time step. In this way, the updated positions, velocities and accelerations are used to evaluate these quantities at the next time step. The velocity-Verlet integration algorithm is used throughout the simulation.

The methodology described above has been implemented into a program known

as the Large-scale Atomic/Molecular Massively Parallel Simulator (LAMMPS) [69]. As discussed in Ch. I, LAMMPS has been used extensively by various research groups and has been used in well over 500 publications. LAMMPS is distributed and maintained by Sandia National Laboratories. All of the simulations presented in this chapter have been performed in LAMMPS and used a time step size of 1 fs.

B. Preliminary Simulations and Results

The following study on various nanostructures has performed a number a different simulations each with the intent to explore different properties. The first set of simulations were designed to use LAMMPS to model an atomistic system and evaluate the structural/mechanical properties of the atomisitic system. Subsequently, simulations on crystals of pure Indium and pure Thallium were performed in order to examine the applicability of different force fields. Finally, a dimensional parametric study was performed to determine if the dimensionality of nanostructures influences the existence of a size effect.

1. Gold

To gain a better understanding of how to use LAMMPS in order to simulate nanostructures, the first step taken was to compare the properties of structures modeled in LAMMPS to known bulk properties. A comparison between known bulk properties and the results obtained through simulation was first accomplished using Gold (Au). Using the built-in MEAM interatomic force field for Au, simulations were performed in order to determine the bulk modulus. The simulations performed to determine the bulk properties of Au used a representative volume element (RVE) of 6 x 6 x 6 unit cells and periodicity in all dimensions. The size of the RVE was large enough to

ensure that each atom would not influence itself while sufficiently small to minimize the computational cost.

One property that can be determined using MD simulations is the bulk modulus of a material. Finding the bulk modulus of the material from MD simulations is useful in determining the applicability of a force field for a given material because the bulk modulus is one of the input parameters when the force field is derived. If the bulk modulus found through MD simulation is close to the published value for the bulk modulus of the material, it is a good indication that the force field used represents the actual material. Using MD simulations the bulk modulus of a material can be determined by finding the slope of the curve for density versus pressure at 0 pressure and using the following equation:

$$K = \rho \frac{\partial P}{\partial \rho}|_{P=0} \tag{4.9}$$

where P is the pressure and ρ is the density of the material. Equation 4.9 is taken from Awasthi *et al.* [84]. The above definition of bulk modulus is consistent with elasticity because the bulk modulus is defined as the resistance to change in volume due to a change in pressure. In Eq. 4.9, the volume is included in the density term. Therefore, Eq. 4.9 exactly corresponds to the definition of bulk modulus for elasticity.

In order to find the bulk modulus, K, the RVE was subjected to compressive and tensile hydrostatic pressure of up to 120,000 bars. The corresponding density versus pressure plot around $P = 0$ is shown in Fig. 21. Using Eq. 4.9 the bulk modulus was evaulated as 163.8 GPa. A published value for the bulk modulus of Au is 167 GPa [85]. The percentage error between the simulation result and the published value for the bulk modulus of Au is approximately 4.2%, which demonstrates that the MEAM force field for Au models the bulk behavior of Au well.

The second criterion used in this study to determine the applicability of a given

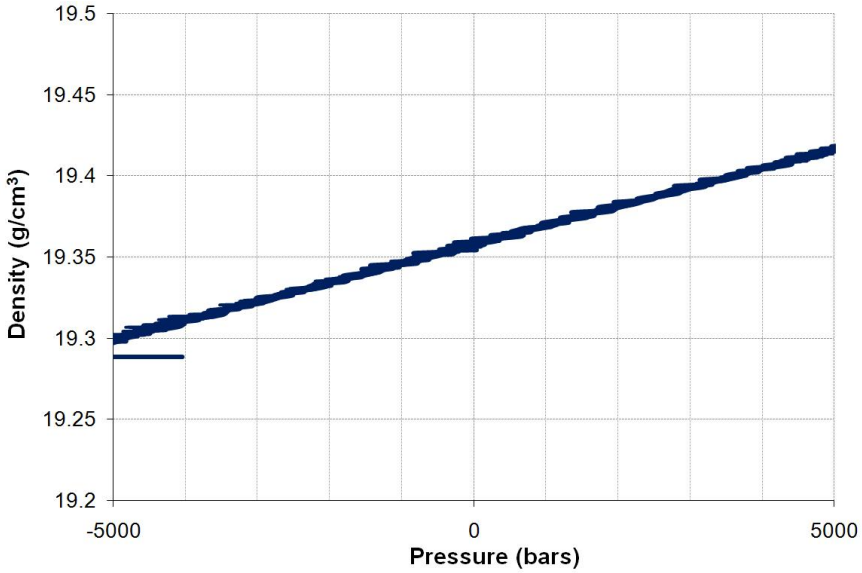

Fig. 21. Density versus pressure for bulk Au.

force field to model a material was the melting temperature. The atoms in a simulation were considered to have melted when the simulation results showed a lack of long range ordering in the atomic positions, as determined through visual inspection of the results using a program called Visual Molecular Dynamics (VMD) [86]. The simulation performed to determine the melting temperature of a material consisted of raising the simulation temperature in 25 °C increments for 2,000 time steps and stabilizing the structure for 18,000 time steps. Each time step lasted for 1 fs. The length of the stabilization was long enough to ensure a fully stabilized system as determined by restarting the simulation after each stabilization period and maintaining the current temperature for an additional 50,000 time steps. Using the above procedure, it was determined that the melting temperature of Au was approximately 1,450 K, which is within 8% error of the published value of 1337 K [85].

2. Indium and Thallium

The focus of this thesis is on Indium-Thallium (InTl) nanowires. Since it was experimentally found that no size effect on the phase transformation of In-21at%Tl nanowires exists, it was decided to use MD simulations to investigate. However, prior to simulating In-21at%Tl nanostructures, it was necessary to ensure that the existing MEAM force fields for pure indium and pure thallium worked properly.

For pure indium, a MEAM force field has been fabricated by Do et al. [87]. In order to verify the claim that the MEAM force field derived by Do et al. predicts accurate properties for indium, two sets of simulations were performed: raising the temperature of an RVE until the atoms behave as if they had melted, and hydrostatic compression/expansion to determine the bulk modulus. The RVE consisted of 10 by 10 by 10 unit cells using the body-centered tetragonal unit cell with lengths $a = b = 3.253$ Åand $c = 4.947$ Å. Using Eq. 4.9, it was found that the bulk modulus of Indium was 41.4 GPa. Comparison between the simulated value for the bulk modulus and the published value of bulk modulus for Indium of 35.3 GPa shows an error of approximately 15% between the published and simulated bulk modulus [88]. The percent error between the published and calculated values is significant, indicating that the indium force field used should not be used in future simulations. A further indication that the force field for In derived by Do et al. should not be used is the fact the, according to the literature the melting point of In is $\approx$ 429 K, but simulations using the In force field derived by Do et al. maintain their long range ordering beyond 800 K.

A similar set of simulations were performed for pure thallium (Tl). For Tl, the MEAM force field used was taken from Baskes and Johnson [89]. The RVE consisted of 10 by 10 by 10 unit cells with a hexagonal close packed crystal structure where

$a = 3.457$. Using Eq. 4.9, it was found that the bulk modulus for Tl predicted by the simulation was 26.2 GPa. According to Olson and Gerward, the bulk modulus of Tl is 44 GPa [28]. The error between the published and calculated bulk modulus is approximately 40%, which indicates that the Tl force field used can not be used for future simulations. Furthermore, the melting temperature as determined using MD simulations was approximately 100 K but the published value of the melting temperature for thallium is 576 K. Therefore, it is clear that the force field derived by Baskes and Johnson for thallium is not correct and should not be used for any further simulations.

C. Dimensionality Parametric Study

As mentioned previously, MD simulations rely on the use of an interatomic force field in order to simulate how atoms behave. In order for the simulations to represent reality, it is necessary to have well developed interatomic force fields. For this study, it would be optimal to have a good interatomic force field for the In-21at%Tl system, however no such force field is available. Furthermore, an attempt was made to develop such a force field, however an insufficient number of input values were available to parameterize the force field. Since the most accurate force field used above was that of Au, the parametric study was performed on Au. As mentioned in the literature review, although bulk Au does not exhibit a phase transformation, Au nanowires do exhibit a phase transformation [26, 23]. Also, since Au has an FCC crystal structure, it is a good analog for InTl since InTl alloys have an FCC crystal structure in the austenitic phase.

In the current section, all the nanostructures are free-standing. The nanostructures representing 0-D nanostructures, 1-D nanostructures, and 2-D nanostructures

are a nanosphere, a nanowire, and a thin film, respectively. All of these nanostructures were simulated in the current study in order to determine if a dimensionality effect exists. Furthermore, since experimental results are available for SMA nanograins, nanowires, and thin films, a true dimensionality study would require the simulation of all these nanostructures.

The parametric study on the dimensionality of nanostructures was performed for two cases. In each case a characteristic length was selected which was utilized by the nanosphere, nanowire, and thin film. The characteristic length selected corresponded to the diameter of the nanosphere, the diameter of the nanowire, and the depth of the thin film. The use of a characteristic length allowed for a direct comparison of the dimensionality of the nanostructures. The characteristic length was 2.45 nm for Case 1 and 3.26 nm for Case 2. These characteristic lengths are related to the size of a Au crystal, respectively representing 6 unit cells and 8 unit cells. For all simulations of the nanowire, the aspect ratio was 10. The exact dimensions for each of the nanostructures examined are shown in Table IV. Ideally one of these characteristic lengths would be approximately the same size as the smallest fabricated nanowire of Ch. III, however due to computational cost such a characteristic length scale could not be used. Simulating a nanowire with a diameter of approximately 10 nm and an aspect ratio of 10 (as used for all simulated nanowires) would require the simulation of over 200,000 atoms, which is approximately the number of atoms used to simulate the thin film of Case 2. However, simulating a thin film with a characteristic length of 10 nm would result in simulating well over 5.6 million atoms. Such a large number of atoms would be too computationally expensive to simulate.

The input script to LAMMPS was consistent throughout the simulations, except for the specification of the structure. The general flow of the simulation was heating by 25 K followed by a stabilization. The exact procedure used for Case 1 is shown in

Table IV. MD simulation structures and dimensions

Dimensionality		*Dimensions*			
		d (nm)	x (nm)	y (nm)	z (nm)
Case 1					
	0	2.45	N/A	N/A	N/A
	1	2.45	N/A	N/A	24.46
	2	N/A	2.45	24.46	24.46
Case 2					
	0	3.26	N/A	N/A	N/A
	1	3.26	N/A	N/A	32.63
	2	N/A	3.26	32.63	32.63

Table V and for Case 2 in Table VI. The number of time steps in each simulation step were chosen to ensure stabilization of the structures after each temperature increment. The earlier simulations performed in this study indicated that 15,000 time steps is long enough to ensure stabilization of the structure. Stabilization of the structure was verified for the earlier simulations by restarting the simulations after the initial stabilization and maintaining the simulation conditions for 50,000 time steps.

In agreement with the results for Au nanowires available in the literature, the simulations performed for Case 1 showed that the Au nanowire exhibited a phase transformation, as shown in Fig. 22. These results indicate a reduction in length of approximately 25%. It should be noted that the transformation occurs primarily between 45 and 70 ps, corresponding to the heating and stabilization of the nanowire to 50 K and 75 K. On the other hand, the nanosphere of Case 1 expands by ap-

Table V. MD simulation steps for case 1

Step	*Action*	*Temperature*		*Number of*
		At Start	*At End*	*Time Steps*
Case 1				
1	Heat	0	1	1000
2	Stabilize	1	1	19000
3	Heat	1	25	3000
4	Stabilize	25	25	12000
5	Heat	25	50	3000
6	Stabilize	50	50	12000
7	Heat	50	75	3000
8	Stabilize	75	75	12000
9	Heat	75	100	3000
10	Stabilize	100	100	12000

Table VI. MD simulation steps for case 2

Step	*Action*	*Temperature*		*Number of*
		At Start	*At End*	*Time Steps*
Case 2				
1	Heat	0	1	1000
2	Stabilize	1	1	19000
3	Heat	1	25	3000
4	Stabilize	25	25	17000
5	Heat	25	50	3000
6	Stabilize	50	50	17000
7	Heat	50	75	3000
8	Stabilize	75	75	17000
9	Heat	75	100	3000
10	Stabilize	100	100	17000
11	Heat	100	125	2000
12	Stabilize	125	125	18000
13	Heat	125	150	2000
14	Stabilize	150	150	18000
15	Heat	150	175	2000
16	Stabilize	175	175	18000
17	Heat	175	200	2000
18	Stabilize	200	200	18000

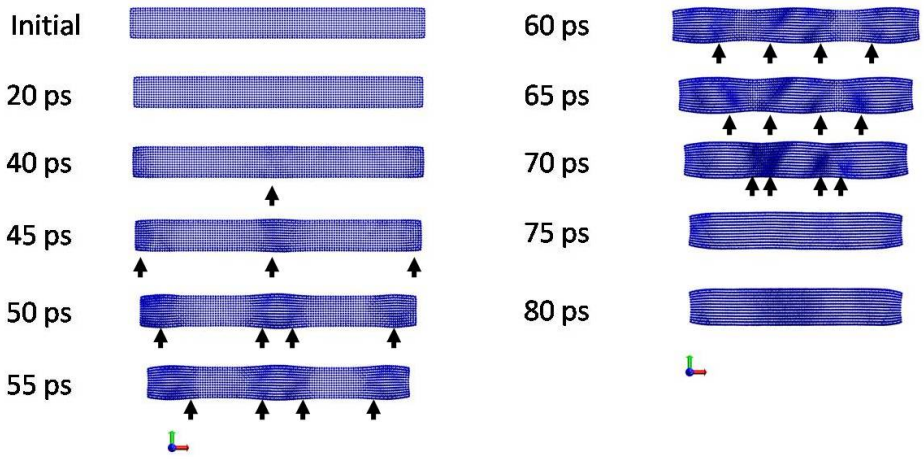

Fig. 22. Case 1: MD simulation of Au nanowire at different time steps (arrows indicate transformation fronts).

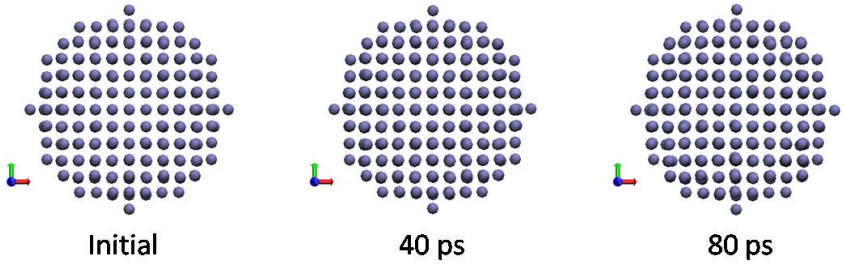

Fig. 23. Case 1: MD simulation of Au nanosphere showing different time steps.

proximately 0.5%, which is expected due to Brownian motion of the atoms. Figure 23 shows that the sphere presents nearly no deformation throughout the simulation. Similarly, as shown in Fig. 24, the thin film of Case 1 presents very little deformation. It does show some minor variations along the edges. Using VMD it was found that the variations along the edges are localized transformation, however the thin film as a whole maintains its initial crystal structure. The localized transformation of the thin film is further explored in the results of Case 2.

The results of Case 2 were similar to the results from Case 1. It should be noted

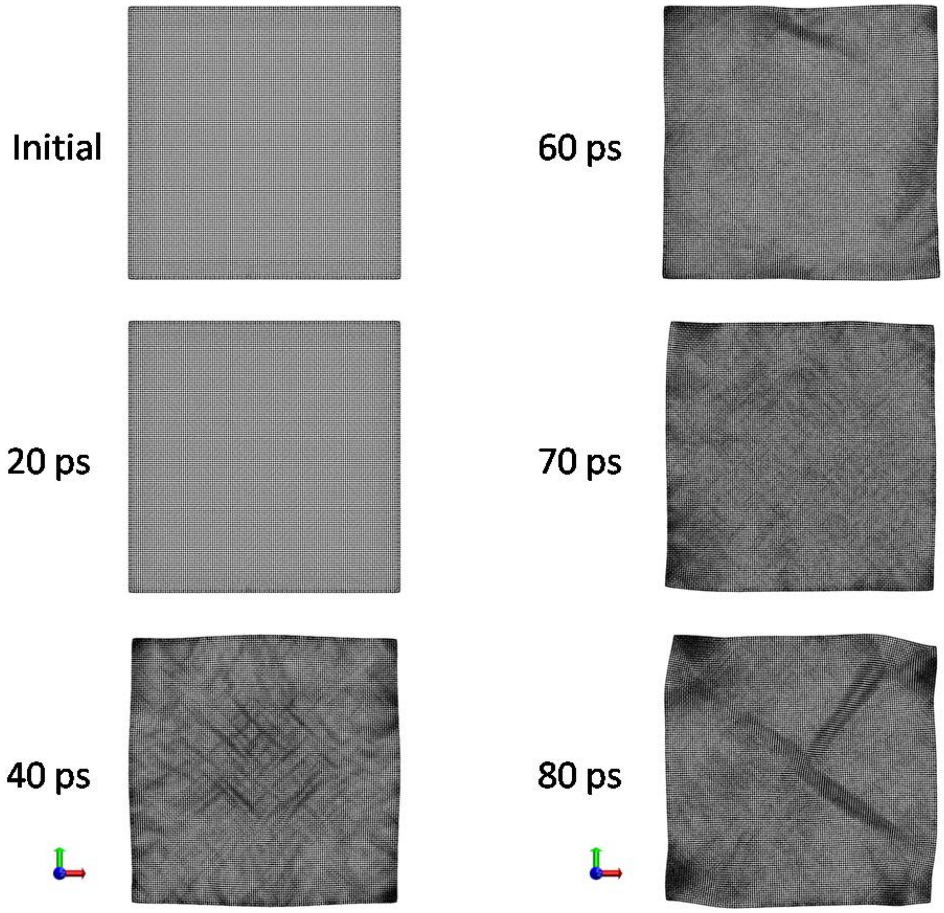

Fig. 24. Case 1: MD simulation of Au thin film at different time steps.

again that the simulations for Case 2 allowed for longer stabilization times at each temperature increment (20,000 time steps instead of 15,000 time steps) and heated each nanostructure to 200 K instead of 100 K. As with Case 1, the nanosphere of Case 2 presents very little deformation throughout the simulation as shown in Fig. 25. Also similar to the result of Case 1 is the result for Case 2 of the nanowire, shown in Fig. 26. The configuration of Case 2 shows a large deformation, on the same order of magnitude in terms of strain as Case 1. The phase transformation for the nanowire of Case 2 occurs primarily between 60 ps and 100 ps, corresponding to heat and stabilization at temperatures of 75 K and 100 K. The temperature range in which the transformation occurs for Case 2 is higher than the transformation temperatures of Case 1. The increase in the transformation temperature is to be expected because the surface atom to volume atom ratio has decreased slightly due to the increase in diameter of the nanowire. The change in the surface atom to volume atom ratio has a more pronounced effect on the thin film of Case 2. Also, it is expected that the transformation shown in Fig. 26 should propogate at the speed of sound which is $3240\frac{m}{s}$ for Au at room temperature [90], however calculations based on the simulation show that the speed of transformation is approximately $1400\frac{m}{s}$. Part of the difference between these two values is that the transformation in the simulation occurs at a much lower temperature (between 75 K and 100 K) than room temperature, which is typically around 293 K. Furthermore, both of these values for the transformation speed and speed of sound are within the same order of magnitude which shows that the transformation speed is probably close to the actual speed of sound at 75 K in Au.

As shown in Fig. 27, the thin film of Case 2 presents less deformation than the thin film of Case 1 (refer to Fig. 24). The reduction in deformation for Case 2 with respect to the deformation of Case 1 is in agreement with Hasmy and Medina who

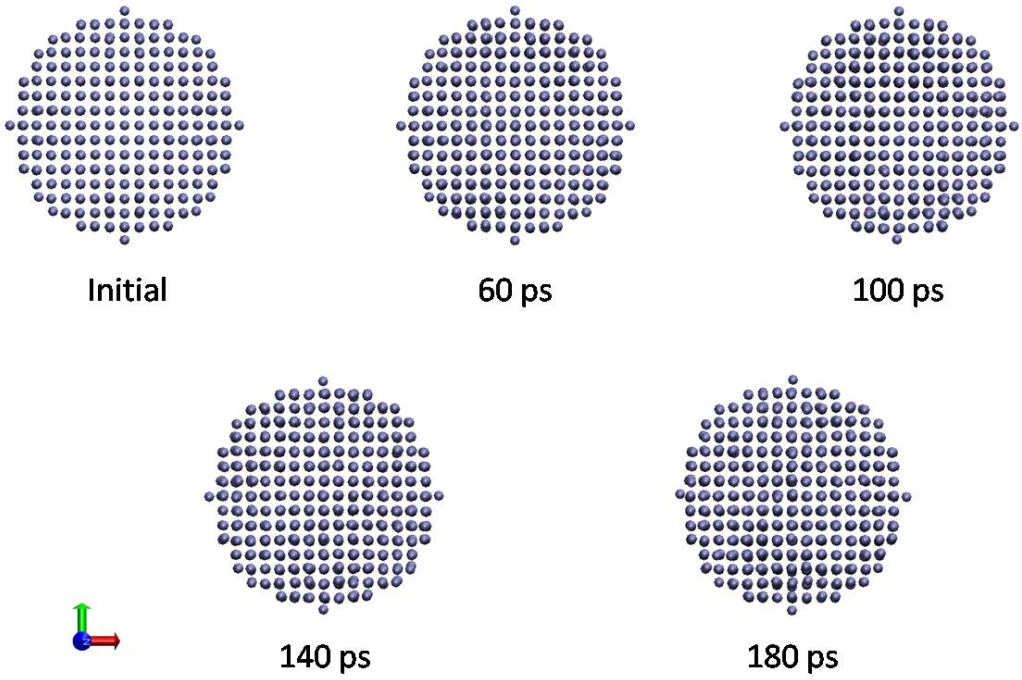

Fig. 25. Case 2: MD simulation of Au nanosphere at different time steps.

state that for Au thin films, there will be transformation if the thin film is less than 8 atomic layers thick [76]. The shear bands shown for the thin films of both Cases 1 and 2 are due to localized transformation. The localized transformation shown for the thin films occur at the same temperature/time range as the transformation in the respective nanowires. However, the localized transformation in the thin films eventually dampens out and the overall crystal structure of the thin films remains the same as the original crystal structure, namely $< 100 >$ FCC.

These MD results indicate a strong dependence on the dimensionality of the nanostructures. No results are currently available for a 3-D nanocube, however it is expected that the results of the 0-D structure would also extend to 3-D structures. The reason why it is expected that the results for the 0-D nanosphere would extend to 3-D structures is based on the fact that in the preliminary investigations, the RVE

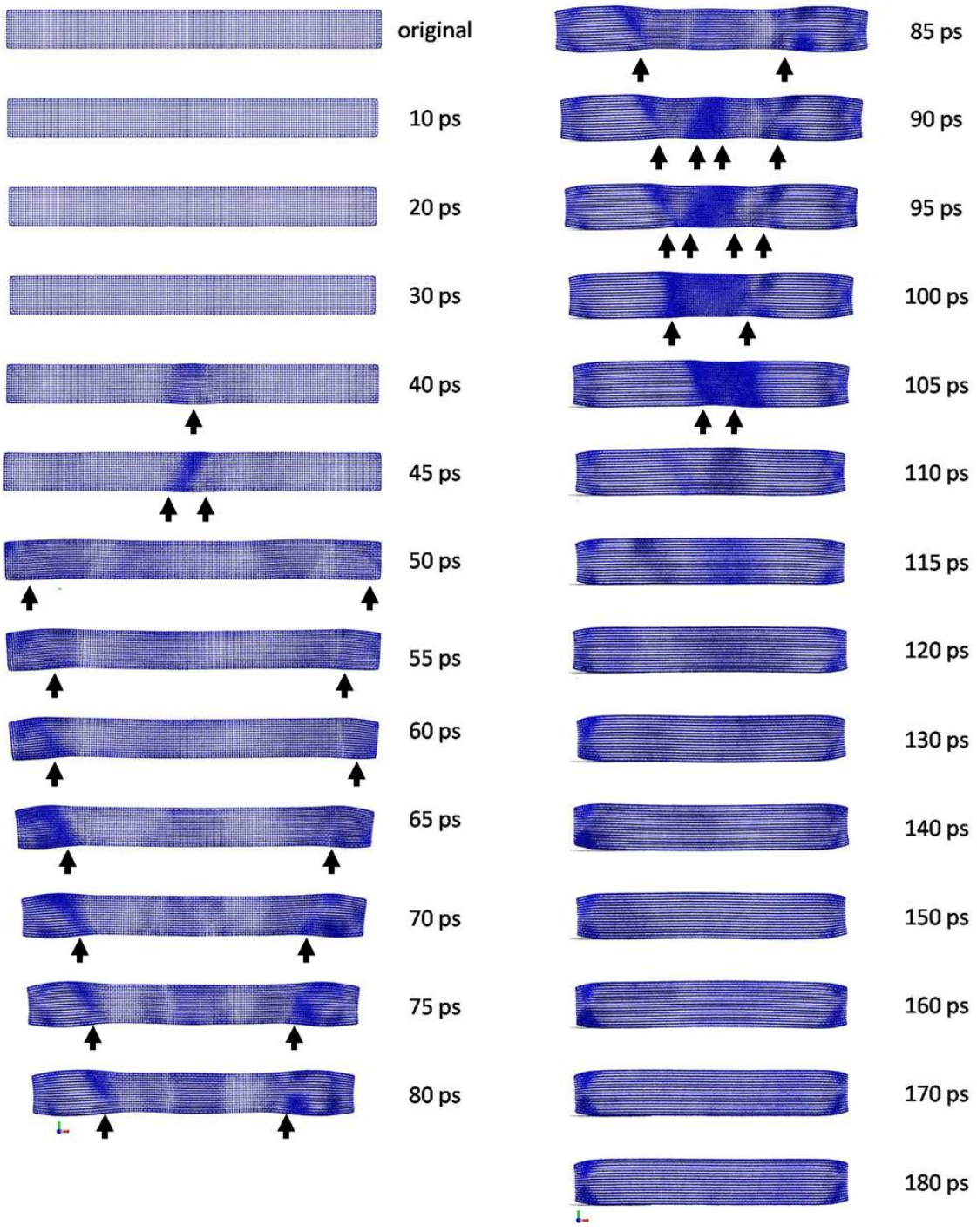

Fig. 26. Case 2: MD simulation of Au nanowire at different time steps (arrows indicate transformation fronts).

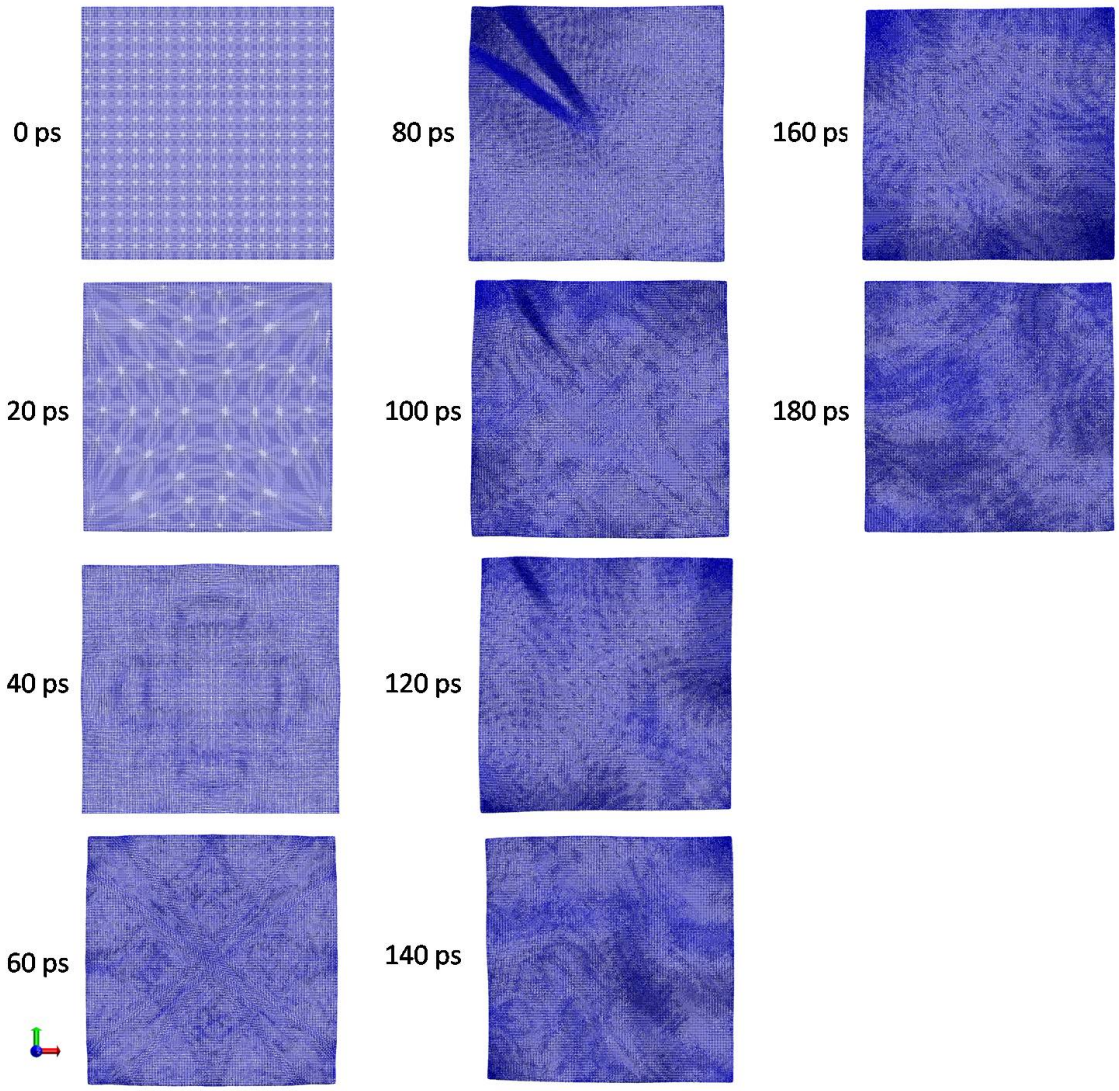

Fig. 27. Case 2: MD simulation of Au thin film at different time steps.

utilized (which was of comparable dimensions to the 0-D nanosphere) exhibited similar properties to the bulk material which is 3-D. The 1-D nanowire exhibits a phase transformation that causes a large change in length, whereas the 0-D nanosphere does not exhibit the phase transformation behavior. Results for the 2-D thin film indicate that it tries to transform, however it is unable to transform similarly to the nanowire. Furthermore, the transformation for 2-D thin films is more highly size dependent than the transformation of the 1-D nanowire. The sensitivity of the thin film is most directly noticed due to the fact that some transformation is observed for the thinner Case 1, where as the thicker Case 2 shows very little transformation. Results from Cases 1 and 2 indicate that although the nanosphere and thicker thin films behave as expected from macroscale observations of Au, the nanowires exhibit a phase transformation.

As reviewed in Ch. I, various other metallic systems exhibit a transformation when these systems are in the form of a nanowire [21, 22]. The existence of a phase transformation for nanowires was further verified for a Ni nanowire. As shown in Fig. 28, there is a phase transformation that propogates through the Ni nanowire. The simulation procedure used to simulate the Ni nanowire is the same procedure as used for Case 2 for the Au nanowire. In the Ni simulation, transformation fronts are clearly observed moving through the nanowire around 50 ps. Since the phase transformation behavior is exhibited for a number of metallic systems, it can therefore be concluded that the above results shown for Au systems can be extended to cover other metallic systems. The proposed extension is a more general statement of the extension proposed by Hasmy and Medina who claimed that their results for Au thin films can be extended to other metallic systems [76]. Therefore, since the above results can be extended to other metallic systems, it can be concluded that SMA nanowires will exhibit a phase transformation throughout the nanoscale.

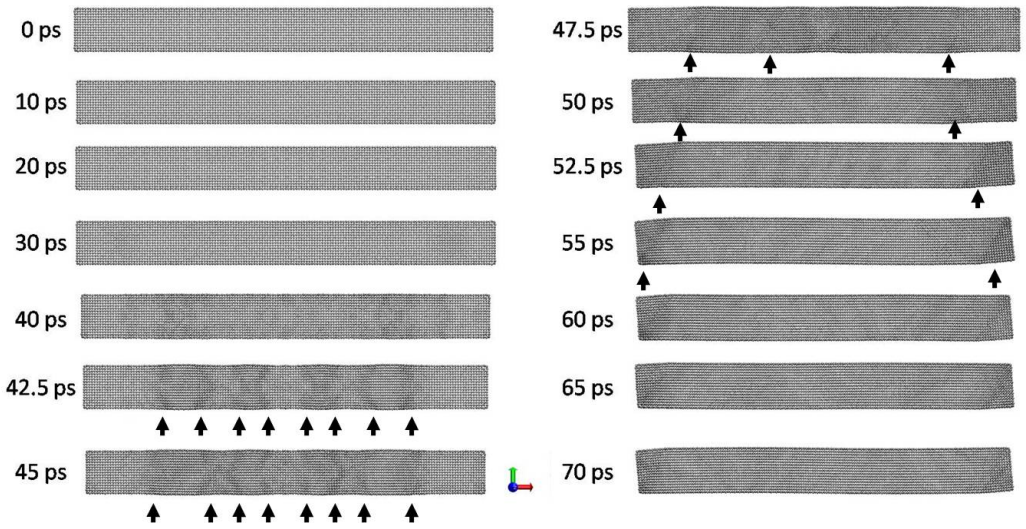

Fig. 28. Ni nanowire showing transformation (arrows indicate transformation fronts).

D. Effect of Constraints on Phase Transformation

Previous experimental studies on SMA nanostructures had all of their nanostructures constrained within or on other material. The SMA nanograins studied by Waitz et al. and Malygin were all constrained within a bulk matrix [14, 15, 18, 20]. Specifically, for the nanograin studies by Waitz et al., the nanograins resulted from high pressure torsion (HPT) on bulk SMA samples and were therefore constrained by the non-transforming matrix surrounding them. Also, the thin films studied by Wan and Komvopoulos were attached to a silica substrate [16]. The silica substrate will act as a constraint on the phase transformation of these SMAs. However, the current study analyzed free-standing SMA nanowires. In order to determine if the imposition of such constraints is responsible for the difference in the results for the SMA nanograins, thin films, and nanowires, further MD simulations were performed. As shown in Sec. C of this chapter, unconstrained Au nanospheres show no transformation, unconstrained Au nanowires show phase transformation, and unconstrained Au thin films show only localized phase transformation, although the overall thin films do not transform. To

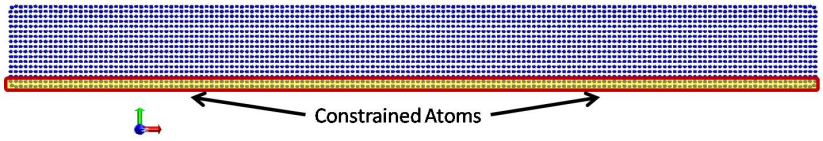

Fig. 29. Nanowire used to simulate effect of constraints on nanostructures.

study the effect of adding a constraint on transforming nanostructures, simulation of the nanowire in Case 2 of the parametric study in Sec. C was repeated but with the addition of a constraint.

The addition of the constraint on the nanowire of Case 2 was accomplished by restricting the bottom two atomic layers from moving, as shown in Fig. 29. The application of such a constraint is similar to the constraint on the experimental thin films because the thin films are constrained from the bottom by a silica substrate. Although such a substrate would tend to restrict the motion of more atoms than only two atomic layers, the two atomic layers constrained in the simulation allows for the free motion of the other atomic layers while maintaining some form of constraint in the overall behavior.

Other than the application of a constraint, the current simulation proceeded in the exact same manner as the nanowire of Case 2 in Sec. C. The results of the simulation with the constraint, however, are different than the results of the unconstrained nanowire. Comparing Fig. 30 to Fig. 26 shows that the constrained nanowire and the unconstrained nanowire both attempt to transform around the same time steps. However, as time progresses, the constrained nanowire is unable to continue the transformation shown by the unconstrained nanowire. It is therefore clear that the application of a constraint on a nanostructure causes a change in the

behavior of the nanostructure.

The current results indicate that a nanostructure which would otherwise transform does not necessarily transform when a constraint is applied on it. As demonstrated in the available literature on constrained SMA nanostructures, the application of a constraint on an SMA nanostructure will eventually inhibit the phase transformation of the SMA due to the constraint. The previous statement also agrees with the experimental results that a free SMA nanowire will transform. As a result of the above studies and the available literature, it is proposed that a free-standing SMA nanowire will transform throughout the nanoscale and that the application of a constraint on phase transforming nanostructures will eventually suppress the phase transformation.

E. Conclusion

Through the use of MD simulations, it has been shown that Au nanowires exhibit a phase transformation where as nanospheres and thin films with equivalent characteristic lengths do not show a phase transformation. Furthermore, the phase transformation observed in Au nanowires is suppressed by the application of a constraint. The phase transformation shown for Au nanowires is different from the bulk behavior of Au as well. Such a transformation has been shown by the current study to exist for Ni nanowires as well and for a range of other metals in other studies. Therefore, since the phase transformation behavior observed was only observed for nanowires of various metallic elements, it can be concluded that all metallic nanowires will exhibit a phase transformation when their diameter is sufficiently small. Furthermore, since SMAs have an inherent phase transformation at the macroscale, these results indicate that SMA nanowires will exhibit a phase transformation throughout the nanoscale.

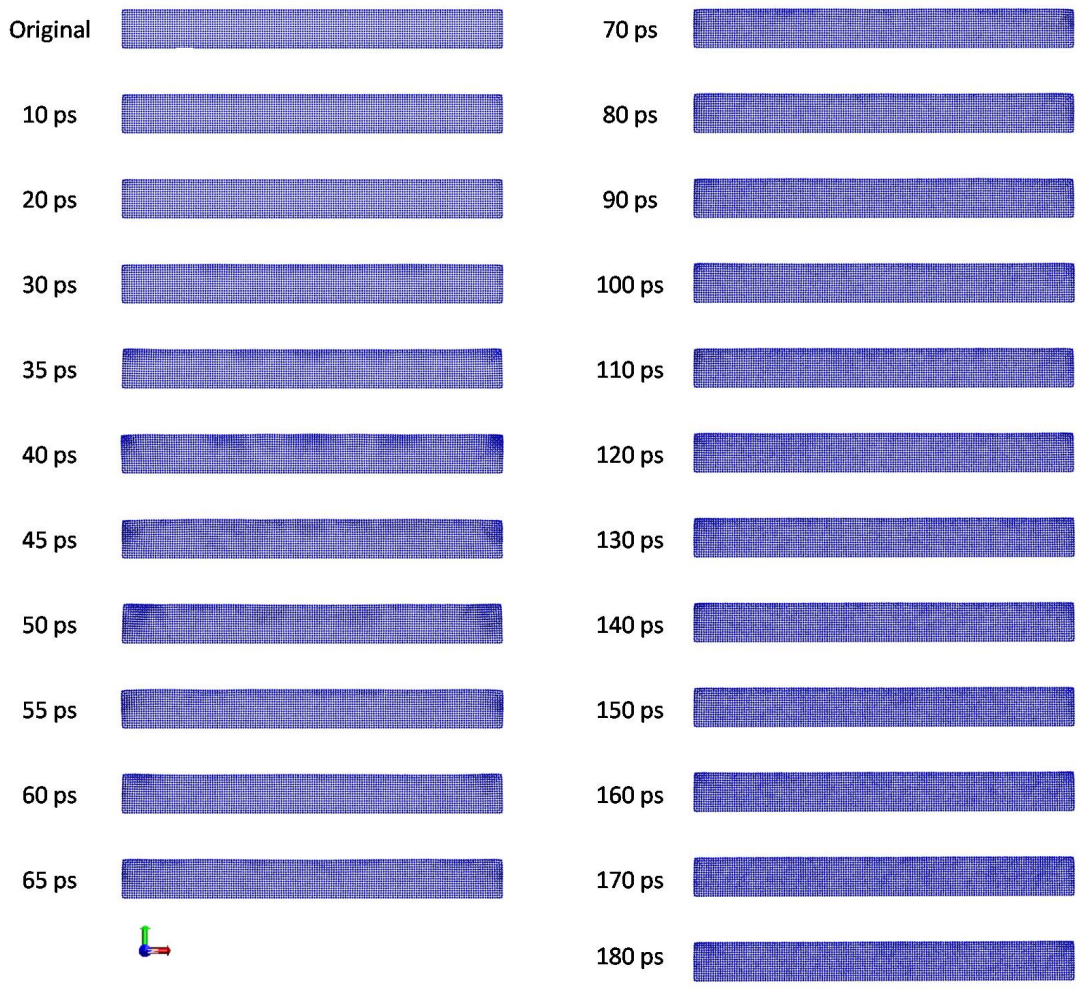

Fig. 30. Simulation of Au nanowire with a constraint. Simulation does not show phase transformation (compare to Fig. 26).

Such a conclusion agrees with the results obtained in Ch. III where a size effect on the phase transformation of an SMA nanowire was not found to exist.

It has been previously proposed that the phase transformation of nanowires is due to the surface energy of a material [23]. All materials have an inherent surface energy due to the fact that at the surface of a material, the energy field is disturbed by the lack of atoms. Therefore, as the size of a material is decreased, the surface energy becomes progressively more pronounced due to the decrease of atoms away from the surfaces. Therefore, the influence of surface energy on the energy of the entire material increases as the size is decreased and may cause the transformation of a nanostructure when the size is sufficiently small. The above parametric study on Au nanostructures has shown that for a non-transforming bulk material, Au nanowires exhibit a phase transformation when their diameter is small enough. Simulation of a Ni nanowire as well as the available literature results indicate that a phase transformation is common to several different metallic materials and therefore SMA nanowires should transform throughout the nanoscale. This result agrees with the experimental results of Ch. III in that free-standing SMA nanowires were found to transform from 650 nm in diameter to 10 nm in diameter.

A further difference between the SMA nanostructures studied in the literature and the current experimental study is the fact that previous studies had their SMA nanostructures constrained. Specifically, studied SMA nanograins and nanocrystals were constrained in a matrix, and the studied SMA thin films were constrained onto a substrate. The current experimental study, however, allows the studied SMA nanowires to be free-standing. To determine the effect of constraining an otherwise phase transforming nanowire, the phase transforming Au nanowire studied in the parametric study was again simulated but with the addition of a constraint. The results of such a simulation indicate that a nanowire which would otherwise transform

no longer transforms with the addition of a constraint. The constrained simulation, in conjunction with previous studies, indicates that a phase transforming SMA nanowire, when constrained, will eventually reach a critical size below which the SMA nanowire will stop transforming.

CHAPTER V

CONCLUSIONS

Through an experimental and numerical characterization of nanowires, it was determined that free-standing SMA nanowires will exhibit a phase transformation throughout the nanoscale. This conclusion was reached by experimentally fabricating and characterizing the phase transformation of In-21at%Tl nanowires with diameters ranging from 650 nm to 10 nm. The nanowires were fabricated using the mechanical pressure injection method and subsequently characterized through transmission electron microscopy analysis with an *in-situ* heating stage. Furthermore, using molecular dynamics, it was found that free-standing metallic nanowires will exhibit a phase transformation which is absent in free-standing metallic nanospheres and thin films. However, in agreement with previous studies on SMA nanostructures, the MD studies performed suggest that upon reaching a critical size, constrained SMA nanostructures will not be able to exhibit a phase transformation.

The first part of this study focused primarily on the fabrication of metallic nanowires using the mechanical pressure injection method. To fabricate metallic nanowires, first an AAO template was fabricated. The steps to fabricate an AAO template are the first anodization, dissolving of the first anodization layer, second anodization, and then a pore widening and heat treatment procedure. The various steps in the fabrication procedure of the AAO templates were analyzed to gain a clearer understanding of the effect of each step. Through scanning electron microscope (SEM) imaging, it was found that the initial AAO fabrication procedure left an irregular surface caused by an inadequat dissolving step. By modifying the dissolving step, the individual processing steps were analyzed to determine how the AAO template fabrication procedure could be modified to yield AAO templates with a different

of nanopore diameters. The primary parameters used to modify the nanopore diameter were the electrolyte and anodization voltage as well as pore widening and heat treatments. By carefully adjusting these parameters, AAO templates with nanopore diameters ranging from 10 nm to 300 nm were fabricated.

Additionally, the above study found a way in which metallic nanowires could be embedded into other nanoscale systems. Embedding metallic nanowires into polymeric nanofibers was accomplished through electrospinning of the Sn nanowires into silica nanofibers. By combining the Sn nanowires with a mixture of spin-on glass intermediate coating IC1-200 solution and polyvinylpyrrolidone, it was found that Sn nanowires could be electrospun into a silica nanofiber. The ability to electrospin these nanowires into polymeric nanofibers provides a new method by which metallic nanowires can be incorporated into a system. Electrical conductivity measurements on the fabricated silica nanofibers found very little change. The lack of change in electrical conductivity has been attributed to the formation of an oxide layer on the Sn nanowires, poor dispersion, and an insufficient quantity of nanowires in the nanofibers.

The focus of this study has been to determine whether there exists a size effect on the phase transformation of shape memory alloy (SMA) nanowires. Due to the need for an alloy with a low melting temperature, the InTl alloys were selected for this study. The literature indicates that for InTl alloys, the austenitic phase has a face-centered cubic (FCC) crystal structure, where as the martensitic phase has a face-centered tetragonal (FCT) crystal structure. First, bulk material of two different compositions of InTl, namely In-21at%Tl and In-26at%Tl, were fabricated. These bulk materials were examined using X-ray diffraction in order to experimentally verify the crystal structure and thus the phase of these alloys at room temperature. The results indicated that the In-21at%Tl alloy had an FCT crystal structure at

room temperature where as the In-26at%Tl alloy had an FCC crystal structure at room temperature. Furthermore it was decided to determine the phase transformation temperature of the In-21at%Tl alloy. The reason that the phase transformation temperature needed to be known was that according to the available literature, a size effect would be expected to decrease the phase transformation temperature. Since In-21at%Tl was already in its martensitic phase at room temperature, a decrease in the phase transformation temperature would be indicated by observing the austenitic phase at room temperature. By using a heating stage within the X-ray diffraction machine, the phase transformation temperature was determined to be between 50 °C and 55 °C.

The study to determine the existence of a size effect on phase transformation of SMA nanowires was conducted by fabricating In-21at%Tl nanowires of various diameters using the fabricated AAO templates to control the nanowire diameter The fabricated In-21at%Tl nanowires were taken to a transmission electron microscope (TEM) to be imaged and to determine the crystal structure of the nanowires. Using selected area electron diffraction (SAED), the crystal structure of all the nanowires tested was determined to be FCT at room temperature. All nanowires for which a heating test was performed exhibited a phase transformation to FCC upon heating and back to FCT upon cooling. These results clearly indicate that no size effect could be found for these nanowires.

In order to attempt to understand these results, molecular dynamic (MD) simulations were performed. Previous results for FCC metals such as Gold (Au) have shown a phase transformation in nanowires which is not present in the bulk material [23]. Using the Modified Embedded Atom Method (MEAM), similar results were shown. However, by increasing or reducing the dimensionality of the Au system, it was found that the phase transformation of Au nanowires was no longer present

in Au nanospheres (0-D) or thin films (2-D). The existence of a phase transformation in free-standing Au nanowires, as well as various other free-standing metallic nanowires, indicates that free-standing SMA nanowires will exhibit a phase transformation throughout the nanoscale. However, upon application of a constraint, the Au nanowire is no longer able to exhibit a phase transformation. The constrained nanowire result can be used to explain why the free-standing SMA nanowires exhibited a phase transformation where as constrained SMA nanograins and thin films are unable to transform. Therefore, the constrained nanowire result indicates that if an SMA nanowire is constrained, there will be a critical size below which the phase transformation is inhibited, thereby providing agreement with other SMA nanostructure experimental evidence.

The described study above is the first step in attempting to determine the nanoscale properties of SMA nanowires. However much more work remains to be accomplished prior to obtaining a complete understanding of the nanoscale behavior of SMA nanowires. Future work on the size effect for SMA nanowires includes the need to perform mechanical testing on SMA nanowires. Mechanical testing of the nanowires should include both constant temperature with varying stress and constant stress with varying temperature loops. Such testing would help to determine whether SMA nanowires maintain the properties of their bulk equivalents or whether the nanoscale has affected their properties. Mechanical testing of nanowires is hard, however, due to the size of the nanowires. One method which could be utilized to test the mechanical properties of the nanowires could involve using an *in-situ* nanomanipulator and a heating stage within an electron microscope. By deforming a SMA nanowire while in its martensitic state and subsequently heating the SMA nanowire, one could determine how much deformation is recovered.

Another task which remains to be accomplished is expanding the above stud-

ies on SMA nanowires research to different SMA compositions. Since the properties of a SMA are highly composition dependent, it would be instructive to fabricate SMA nanowires from different compositions. However, the fabrication of nanowires from different compositions would likely require the use of different nanowire fabrication procedures as well. The use of different compositions and different fabrication methodologies could allow for the fabrication and use of various different SMA nanowires. According to macroscopic studies, the volume change for InTl alloys is only 0.016% [54], however alloys such as Nickel Titanium deform by as much as 10% [4]. Thus, the fabrication of SMA nanowires using different compositions could lead to the widespread use of SMA nanowires.

In summary, various metallic nanowires have been fabricated through the use of the mechanical pressure injection method. The fabrication procedure of the AAO templates used in the mechanical pressure injection method, was studied and modifications to the AAO fabrication procedure were implemented to allow the fabrication of nanowires with various different diameters. The phase transformation of In-21at%Tl nanowires was characterized through the use of a TEM and the results indicated that no size effect could be found for nanowires ranging in diameter from 650 nm to 10 nm. Furthermore, through the use of MD simulations, it was shown that free-standing SMA nanowires are expected to exhibit a phase transformation throughout the nanoscale. However, the application of a constraint on SMA nanowires is likely to eventually inhibit the phase transformation, which is in agreement with previous experimental results on SMA nanostructures.

REFERENCES

[1] M. Schwartz (Ed.), Smart Materials, CRC Press, Boca Raton, FL, 2009.

[2] S. Cleevely, Piezoelectric polymeric coatings application in computer devices and sensors, Materials World 11 (2003) 27–28.

[3] A. Arnau, Piezoelectric transducers and applications, Springer-Verlag, New York, 2008.

[4] D. Lagoudas (Ed.), Shape Memory Alloys: Modeling and Engineering Applications, Springer-Verlag, New York, 2008.

[5] A. Srinivasan, D. McFarland, Smart Structures: Analysis and Design, Cambridge University Press, Cambridge, UK, 2001.

[6] K. Otsuka, C. M. Wayman, Shape Memory Materials, Cambridge University Press, Cambridge, UK, 1999.

[7] D. A. Horsley, R. Horowitz, A. P. Pisano, Microfabricated electrostatic actuators for hard disk drives, IEEE-ASME Transactions on Mechatronics 3 (1998) 175–183.

[8] K. J. Gabriel, Microelectromechanical systems, Proceedings of IEEE 86 (1998) 1534–1535.

[9] S. Henry, D. V. McAllister, M. G. Allen, M. R. Prausnitz, Microfabricated microneedles: A novel approach to transdermal drug delivery, Journal of the Pharmaceutical Society 87 (1998) 922–925.

[10] M. Gad-el Hak (Ed.), MEMS: Design and Fabrication, Taylor & Francis, Boca Raton, Florida, 2005.

[11] P. Chu, S. Lee, S. Park, MEMS: The path to large optical crossconnects, Communications Magazine, IEEE 30(3) (2002) 80–87.

[12] J. Gardner, V. Varadan, O. Awadelkarim, Microsensors, MEMS, and Smart Devices, John Wiley & Sons, New York, 2001.

[13] S. Lyshevski, MEMS and NEMS: System, Devices, and Structures, Taylor & Francis, Boca Raton, Florida, 2002.

[14] G. Malygin, Nanoscopic size effects on martensitic transformations in shape memory alloys, Physics of the Solid State 50(8) (2008) 1538–1543.

[15] T. Waitz, T. Antretter, F. D. Fischer, N. K. Simha, H. P. Karnthaler, Size effects on the martensitic phase transformation of niti nanograins, Journal of the Mechanics and Physics of Solids 55 (2007) 419–444.

[16] D. Wan, K. Komvopoulos, Thickness effect on thermally induced phase transformations in sputtered titanium-nickel shape-memory films, Journal of Materials Research 20 (2005) 1606–1612.

[17] C. Lexcellent, S. Moyne, A. Ishida, , S. Miyazaki, Deformation behaviour associated with the stress-induced martensitic transformation in Ti-Ni thin films and their thermodynamical modelling, Thin Solid Films 324(1-2) (1998) 184–189.

[18] T. Waitz, W. Pranger, T. Antretter, F. Fischer, H. Karnthaler, Competing accommodation mechanisms of the martensite in nanocrystalline NiTi shape memory alloys, Materials Science and Engineering: A 481-482 (2008) 479–483.

[19] Y. Fu, H. Du, W. Huang, S. Zhang, M. Hu, TiNi-based thin films in MEMS applications: A review, Sensors and Actuators A: Physical 112(2-3) (2004) 395–408.

[20] T. Waitz, V. Kazykhanov, H. Karnthaler, Martensitic phase transformation in nanocrystalline NiTi studied by TEM, Acta Materialia 52(7) (2004) 137–147.

[21] W. Liang, M. Zhou, F. Ke, Shape memory effect in copper nanowires, Nano Letters 5 (2005) 2039–2043.

[22] H. Park, C. Ji, On the thermomechanical deformation of silver shape memory nanowires, Acta Materialia 54(10) (2006) 2645–2654.

[23] J. Diao, K. Gall, , M. Dunn, Surface stress driven reorientation of gold nanowires, Physical Review B 70(7) (2004) 075413.

[24] J. Diao, K. Gall, M. L. Dunn, Surface-stress-induced phase transformation in metal nanowires, Nature Materials 2 (2003) 656–660.

[25] H. S. Park, J. A. Zimmerman, Stable nanobridge formation in $< 110 >$ gold nanowires under tensile deformation, Scripta Materialia 54 (2006) 1127–1132.

[26] H. Park, K. Gall, J. Zimmerman, Shape memory and pseudoelasticity in metal nanowires, Physical Review Letters 95 (2005) 255504.

[27] J. Jorritsma, A. M. Gijs, J. M. Kerkhof, J. G. H. Stienen, General technique for fabricating large arrays of nanowires, Nanotechnology 7 (1996) 263–265.

[28] E. Olson, G. C. Spalding, A. M. Goldman, M. J. Rooks, New method for fabricating ultra-narrow metallic wires, Applied Physics Letters 65 (1994) 2740–2742.

[29] J. M. Gibson, Reading and writing with electron beams, Physics Today 50(10) (1997) 56–61.

[30] S. Matsui, Y. Ochiai, Focused ion beam applications to solid state devices, Nanotechnology 7 (1996) 247–258.

[31] A. M. Haghiri-Gosnet, C. Vieu, G. Simon, M. Mejlas, F. Carcenac, H. Launois, Nanofabrication at a 10 nm length scale: Limits of lift-off and electroplating transfer processes, Journal de Physique IV 9 (1999) Pr2.133–Pr2.141.

[32] S. H. Hong, J. Zhu, C. A. Mirkin, Multiple ink nanolithography: Toward a multiple-pen nano-plotter, Science 286 (1999) 523–525.

[33] J. A. Dagata, Device fabrication by scanned probe oxidation, Science 270 (1995) 1625–1626.

[34] T. Gao, G. Meng, J. Zhang, S. Sun, L. Zhang, Template synthesis of y-junction metal nanowires, Applied Physics A: Materials Science & Processing 74 (2002) 403–406.

[35] V. M. Fedosyuk, O. I. Kasyutich, W. Schwarzacher, Granular agco and agcuco nanowires, Journal of Magnetism and Magnetic Materials 198-199 (1999) 246–247.

[36] H. Masuda, K. Fukuda, Ordered metal nanohole arrays made by a two-step replication of honeycomb structures of anodic alumina, Science 268 (1995) 1466–1468.

[37] C. J. Brumlik, V. P. Menon, C. R. Martin, Template synthesis of metal microtubule ensembles utilizing chemical, electrochemical, and vacuum deposition techniques, Journal of Materials Research 9 (1994) 1174–1183.

[38] V. M. Cepak, C. R. Martin, Preparation and stability of template-synthesized metal nanorod sols in organic solvents, Journal of Physical Chemistry B 102 (1998) 9985–9990.

[39] S. H. Chen, C. C. Chen, Z. P. Luo, C. G. Chao, Fabrication and characterization of eutectic bismuth-tin (bi-sn) nanowires, Materials Letters 63 (2009) 1165–1168.

[40] C. Chen, Y. Bisrat, Z. Luo, R. Schaak, C. Chao, D. Lagoudas, Fabrication of single-crystal tin nanowires by hydraulic pressure injection, Nanotechnology 17 (2006) 367–374.

[41] S. H. Chen, C. C. Chen, C. G. Chao, Novel morphology and solidification behavior of eutectic bismuth-tin (bi-sn) nanowires, Journal of Alloys and Compounds 481 (2009) 270–273.

[42] Y. Bisrat, Z. Luo, D. Davis, D. Lagoudas, Highly ordered uniform single-crystal Bi nanowires: Fabrication and characterization, Nanotechnology 18 (2007) 395601.

[43] J. S. Lin, C. C. Chen, E. W. G. Diau, T. F. Liu, Fabrication and characterization of eutectic gold-silicon (au-si) nanowires, Journal of Materials Processing Technology 206 (2007) 425–430.

[44] H. Masuda, F. Hasegawa, S. Ono, Self-ordering of cell arrangement of anodic porous alumina formed in sulfuric acid solution, Journal of the Electrochemical Society 144 (1997) L127–L130.

[45] H. Masuda, K. Yada, A. Osaka, Self-ordering of cell configuration of anodic porous alumina with large-size pores in phosphoric acid solution, Japanese Journal of Applied Physics 37 (Part 2) (1998) L1340–L1342.

[46] O. Jessensky, F. Muller, U. Gosele, Self-organized formation of hexagonal pore arrays in anodic alumina, Applied Physics Letters 72 (1998) 1173–1175.

[47] A. P. Li, F. Muller, A. Birner, K. Nielsch, U. Gosele, Hexagonal pore arrays with a 50 - 420 nm interpore distance formed by self-organization in anodic alumina, Journal of Applied Physics 84 (1998) 6023–6026.

[48] X. Y. Zhang, L. D. Zhang, Y. Lei, L. X. Zhao, Y. Q. Mao, Fabrication and characterization of highly ordered au nanowire arrays, Journal of Materials Chemistry 11 (2001) 1732–1734.

[49] A. Formhals, Process and apparatus for preparing artificial threads, Patent, US 1,975,504 (10 1934).

[50] S. Chand, Review: Carbon fibers for composites, Journal of Materials Science 35 (2000) 1303–1313.

[51] Z. M. Huang, y. Z. Zhang, M. Kotaki, S. Ramakrishna, A review on polymer nanofibers by electrospinning and their applications in nanocomposites, Composites Science and Technology 63 (2003) 2223–2253.

[52] M. Bouville, R. Ahluwalia, Microstructure and mechanical properties of constrained shape-memory alloy nanograins and nanowires, Acta Materialia 56(14) (2008) 3558–3567.

[53] K. Saitoh, W. K. Liu, Molecular dynamics study of surface effect on martensitic cubic-to-tetragonal transformation in Ni-Al alloy, Computational Materials Science 46 (2009) 531–544.

[54] O. Nittono, Y. Koyama, Phenomenological considerations of phase transformations in indium-rich alloys, Japanese Journal of Applied Physics 21(5) (1982) 680–687.

[55] T. B. Massalski (Ed.), Binary Alloy Phase Diagrams, American Society for Metals, Metals Park, Ohio, 1986.

[56] D. E. Hodgson, J. W. Brown, Using Nitinol Alloys, San Jose, California, Shape Memory Applications, Inc., 2000.

[57] M. Brassington, G. Saunders, Vibrational anharmonicity and the elastic phase transition of indium-thallium alloys, Proceedings of the Royal Society of London 387 (1983) 289–310.

[58] T. Jaglinski, P. Frascone, B. Moore, D. Stone, R. Lakes, Internal fricition due to negative stiffness in the indium-thallium martensitic phase transformation, Philosophical Magazine 86(27) (2006) 4285–4303.

[59] Z. S. Basinski, J. W. Christian, Experiments on the martensitic transformation in single crystals of indium-thallium alloys, Acta Metallurgica 2 (1954) 161–166.

[60] H. Schumann, Crystallography of the martensitic transformation in indium-thallium alloys, Crystal Research & Technology 17 (1982) 1031–1039.

[61] K. Bhattacharya, Microstructure of Martensite: Why it Forms and How it Gives Rise to the Shape-Memory Effect, Cambridge University Press, Cambridge, UK, 2003.

[62] P. Hohenberg, W. Kohn, Inhomogeneous electron gas, Physical Review 136 (1964) B864–B871.

[63] W. Kohn, L. J. Sham, Self-consistent equations including exchange and correlation effects, Physical Review 140 (1965) A1133–A1138.

[64] R. G. Parr, Density functional theory, Annual Review of Physical Chemistry 34 (1983) 631–656.

[65] M. A. L. Marques, E. K. U. Gross, Time-dependend density functional theory, Annual Review of Physical Chemistry 55 (2004) 427–455.

[66] D. P. Landau, K. Binder, A guide to Monte Carlo Simulations in Statistical Physics, Cambridge University Press, Cambridge, UK, 2000.

[67] J. R. Rustad, A. R. Felmy, B. P. Hay, Molecular statics calculations for iron oxide and oxyhydroxide minerals: Toward a flexible model of the reactive mineral-water interface, Geochimica et Cosmochimica Acta 60 (1996) 1553–1562.

[68] H. Liang, M. Upmanyu, H. Huang, Size-dependent elasticity of nanowires: Non-linear effects, Physical Review B 71 (2005) 241403.

[69] S. J. Plimpton, Fast parallel algorithms for short-range molecular dynamics, Journal of Computational Physics 117 (1995) 1–19.

[70] L. Sandoval, H. Urbassek, Solid-solid phase transitions in fe nanowires induced by axial strain, Nanotechnology 20 (2009) 325704.

[71] Q. Cheng, H. A. Wu, Y. Wang, X. Wang, Pseudoelasticity of cu-zr nanowires via stress-induced martensitic phase transformations, Applied Physics Letters 95 (2009) 021911.

[72] D. Farkas, D. Roqueta, A. Vilette, K. Ternes, Atomistic simulations in ternary ni-ti-al alloys, Modelling and Simulation in Materials Science and Engineering 4 (1996) 359–369.

[73] M. S. Daw, M. I. Baskes, Embedded-atom method: Derivation and application to impurities, surfaces, and other defects in metals, Physical Review Letters B 29 (1984) 64436453.

[74] M. I. Baskes, Application of the embedded-atom method to covalent materials: A semiempriical potential for silicon, Physical Review Letters 59 (1987) 2666–2669.

[75] C. Kuo, P. Clancy, Meam molecular dynamics study of a gold thin film on a silicon substrate, Surface Science 551 (2004) 39–58.

[76] A. Hasmy, E. Medina, Thickness induced structural transition in suspended fcc metal nanofilms, Physical Review Letters 88 (2002) 096103.

[77] W. Lee, B. Park, D. Kim, D. Ahn, Y. Park, S. Lee, K. Lee, Nanostructure-dependent water-droplet adhesiveness change in superhydrophobic anodic aluminum oxide surfaces: From highly adhesive to self-cleanable, Langmuir 26 (2010) 1412–1415.

[78] M. Abramoff, P. Magelhaes, S. Ram, Image processing with ImageJ, Biophotonics International 11 (2004) 36–42.

[79] D. Young, Computational chemistry: A practical guide for applying techniques to real world problems, John Wiley & Sons, New York, 2001.

[80] M. S. Daw, M. I. Baskes, Semiempirical, quantum mechanical calculation of hydrogen embrittlement in metals, Physical Review Letters 50 (1983) 12851288.

[81] M. I. Baskes, J. S. Nelson, A. F. Wright, Semiempirical modified embedded-atom potentials for silicon and germanium, Physical Review B 40 (1989) 6085–6100.

[82] M. I. Baskes, Modified embedded-atom potentials for cubic materials and impurities, Physical Review B 46 (1992) 2727–2742.

[83] W. C. Swope, H. C. Andersen, P. H. Berens, K. R. Wilson, A computer simulation method for the calculation of equilibrium constants for the formation of physical

clusters of molecules: Application to small water clusters, Journal of Chemical Physics 76 (1982) 637–649.

[84] A. Awasthi, D. Lagoudas, D. Hammerand, Modeling of graphene-polymer interfacial mechanical behavior using molecular dynamics, Modelling and Simulation in Materials Science and Engineering 17 (2009) 015002.

[85] D. Heinz, R. Jeanloz, The equation of state of the gold calibration standard, Journal of Applied Physics 55 (1984) 885–893.

[86] W. Humphrey, A. Dalke, K. Schulten, VMD: Visual molecular dynamics, Journal of Molecular Graphics 14 (1996) 33–38.

[87] E. C. Do, Y.-H. Shin, B.-J. Lee, A modified embedded-atom method interatomic potential for indium, Computer Coupling of Phase Diagrams and Thermochemistry 32 (2008) 82–88.

[88] K. Takemura, Effect of pressure on the lattice distortion of indium to 56 gpa, Physical Review B 44 (1991) 545–549.

[89] M. I. Baskes, R. A. Johnson, Modified embedded atom potentials for hcp metals, Modelling and Simulation in Materials Science and Engineering 2 (1994) 147–163.

[90] J. Hodak, A. Henglein, G. Hartland, Size dependent properties of au particles: Coherent excitation and dephasing of acoustic vibrational modes, Journal of Chemical Physics 111 (1999) 8613–8621.

VITA

Francis Randall Phillips is the first child of Jonathan and Sylvie, and brother to Cynthia. He is married to his wife Melissa. Francis attended Texas A&M University and completed a B.S. in Aerospace Engineering in May of 2008. He then enrolled in the graduate program in Materials Science and Engineering at Texas A&M University in the fall of 2008, where he has worked under the guidance of Dr. Dimitris C. Lagoudas. He received his M.S. degree in Materials Science and Engineering in August of 2010. His research interests include the fabrication and characterization of active nanostructures, with a particular focus on Shape Memory Alloys. An extended resume can be found at http://smart.tamu.edu. Mr. Phillips can be reached at:

Texas A&M University
Department of Aerospace Engineering
College Station, TX 77843-3141

His email address is phillips.francis@gmail.com.

The typist for this thesis was Francis Randall Phillips.